Thermally tuned TeO_2-Si Microdisk Resonators

Thermally tuned TeO_2-Si Microdisk Resonators

By Parimal Edke, B.A.Sc.

A Thesis Submitted to the School of Graduate Studies in the Partial Fulfillment of the Requirements for the Degree Master of Applied Science

McMaster University

Master of Applied Science (2022)

Hamilton, Ontario (Department of Engineering Physics)

TITLE: Thermally tuned TeO_2-Si Microdisk Resonators

AUTHOR: Parimal Edke B.A.Sc. (McMaster University)

SUPERVISOR: Dr. Jonathan Bradley

NUMBER OF PAGES: x, 90

Abstract

In this research, we design and characterize thermally tuned hybrid tellurium oxide coated silicon (TeO_2-Si) microdisk resonators for the development of tunable on chip lasers. Several heater designs are proposed that are compatible with standard silicon photonics foundry processes and the requirement to deposit TeO_2 onto the fabricated chips in post-processing. The devices are designed using simulation software packages such as Lumerical MODE and HEAT to simulate the mode profiles and thermo-optic coefficients of the microdisk resonators and the heating profiles of the various heater designs. The devices are laid out using the Luceda IPKISS Photonics Design Platform and fabricated at the AMF silicon photonics foundry. TeO_2 is then deposited onto the fabricated chips at McMaster University in a single post-processing step via reactive radio frequency magnetron sputtering. Passive optical transmission measurements are performed to characterize the intrinsic Q-factors, loss and FSR of the microdisks. This is followed by resonance tuning measurements to characterize the tuning efficiencies of each of the heater designs presented in this thesis. The performances of each of the heater designs are then discussed and compared.

Acknowledgements

So many people to thank!

Dr. Jonathan Bradley, my supervisor, who provided invaluable guidance and support especially during the tough Covid-19 pandemic.

Henry Frankis, for training me on the thermal tuning experimental setup and developing the Matlab and Luceda scripts that made many daunting tasks trivial.

Khadijeh Miarabbas Kiani, for always taking time out of your busy schedule to help me with my experiments whenever I felt lost.

Bruno Luis Segat Frare, for performing all my film depositions with utmost care and excellence.

Dawson Bonneville, for training me on the passive experimental setup during the tough Covid-19 pandemic restrictions.

Cameron Naraine, for providing an excellent template and reference for this thesis.

My family (mom, dad and my sister Parinita) for always supporting me in all my endeavours.

Finally, to anyone I may have missed, thank you for everything. This thesis could not have been completed without you.

Contents

List of Figures

List of Tables

Chapter 1

Introduction

1.1 Silicon photonics in integrated optics

The interest in silicon as an optical platform for integrated optics has been increasing rapidly since the early 21st century. The primary reason for this interest is to utilize the huge amount of research and development, both in terms of time and resources, that has gone into developing silicon as the material of choice in the microelectronics industry [1]. The technology for manufacturing silicon devices at the micro and nanoscale is extremely mature. Silicon is optically transparent at wavelengths greater than 1.1 μm which means it can be used in all the common telecommunication bands. Silicon's refractive index ($n \approx 3.5$) is also much higher than that of silicon dioxide ($n \approx 1.45$) and air ($n \approx 1$) which enables the creation of extremely compact photonic devices. The plasma dispersion effect can also be effectively exploited in silicon to make efficient and high speed active photonic devices such as optical modulators [2]. However, silicon has some major drawbacks. The primary drawback of silicon is its indirect bandgap which makes it a poor light

emitter. Silicon waveguides also exhibit higher linear and nonlinear optical propagation loss than other dielectric and fiber-based waveguide platforms. Silicon also does not possess a first order electro-optic effect, known as Pockel's effect, that is characteristically used to create ultra fast optical modulators [3]. Despite these drawbacks, the potentially huge economic benefits of using silicon in integrated photonics has fuelled massive research and development efforts to overcome these challenges.

Several research directions have been explored to create light sources on silicon chips. One approach to create efficient electrically pumped light sources is to integrate III-V materials with silicon. Many approaches to achieve this have been explored such as bonding III-V chips onto silicon chips [4] and epitaxially growing III-V materials directly onto silicon [5]. However, these approaches are challenging due to the lattice mismatch between III-V materials and silicon. Silicon Raman lasers have been developed that are fully integrable and tunable but exhibit low efficiency and require a tunable pump light source [6–8]. Another promising approach is the incorporation of rare-earth ions such as erbium and thulium onto silicon waveguides to create efficient on-chip lasers and amplifiers [9, 10]. This is the main approach that is pursued by our research group.

1.2 Tellurium oxide as a cladding material

Tellurium oxide (TeO_2) is a very attractive material for integrated photonics. It has a high refractive index of $n \approx 2.1$. It is transparent from 0.4 μm to 5 μm with low dispersion [11]. TeO_2 waveguides have been demonstrated to have low propagation losses of ≈ 0.1 dB/cm [12, 13]. It has high rare-earth ion solubility, low

quenching, large emission bandwidths and low phonon energies [11, 13–15]. TeO_2 also has a high nonlinear refractive index of $n_2 = 1.3 \times 10^{-18} m^2/W$ at a wavelength of 1900 nm [13, 16]. All these properties lead to TeO_2 being an excellent material for both passive and active photonic devices.

TeO_2 has several advantages over SiO_2 as a cladding material for silicon waveguides. First and foremost, the lower refractive index contrast between TeO_2 ($n \approx 2.1$) and Si ($n \approx 3.5$) than compared to the refractive index contrast between SiO_2 ($n \approx 1.45$) and Si leads to significantly lower scattering losses at the core cladding interface, which can allow for lower loss waveguides [17, 18]. Secondly, the lower index contrast leads to an increase in the overlap of the mode with the TeO_2 cladding. This is important for active devices in order to increase the interaction of the mode with the rare-earth-doped TeO_2 gain material which leads to higher gain. Our group has demonstrated several active hybrid TeO_2-Si and TeO_2-Si_3N_4 devices such as erbium based and thulium based lasers and amplifiers [9, 19, 20].

1.3 Travelling wave resonators

Travelling wave resonators (TWR), such as microrings and microdisks, are important and versatile photonic devices. They consist of a closed path for light to travel through which leads to the light interfering with itself. In order for light to remain in the resonator, it must interfere constructively with itself. Hence, a TWR only supports light at certain resonant frequencies [21]. A TWR by itself is not very useful. In order to be useful, it must interact with the external world by means of a bus waveguide. When placed next to a bus waveguide which evanescently

couples light to and from the TWR, TWR's can be used to trap light within them for long periods of time and concentrate the light to intensities that are far greater than the initial excitation. TWR's have many useful applications. Their very selective resonant frequencies can be used to design spectral filters and switches [22]. Since their resonant frequencies are extremely sensitive to the effective index of the TWR which depends on the cladding refractive index, they can be used to design biological sensors [23]. The strong dispersion of TWR's near their resonant frequencies can be used to generate true time delay [24]. The extremely high intensity that can be achieved by light constructively interfering with itself in a TWR can be used for non-linear applications [25]. The closed light path in a TWR can be used to design laser cavities [9].

TWR's are very selective in their allowed frequencies. Factors such as fabrication variations can have a large effect on the resonant frequencies of a TWR. Furthermore, for many of the applications mentioned above, TWR's would not be very useful if we could not have some control over the resonant frequencies. Fortunately, silicon has a large thermo-optic coefficient of about $1.8 \times 10^{-4} K^{-1}$ at a wavelength of 1550 nm [26]. This means that the refractive index of silicon changes slightly with temperature. This property allows us to control the refractive index of the silicon TWR by heating it, thus controlling the resonant frequencies. This enables us to design tunable filters and sensors, variable true time delay devices, modulators and tunable lasers. In this project, we design thermally tuned hybrid TeO_2-Si microdisk resonators for their potential application in tunable lasers. We explore various heater designs to measure and compare their resonance tuning performance.

1.4 Thesis outline

Chapter 2 reviews the background and theory behind optical waveguides, microdisk resonators and thermal tuning of microdisk resonances. Equations for evaluating the performance of the various heater designs presented in this thesis are discussed at the end of the chapter.

Chapter 3 describes the fabrication process used to manufacture our devices. Following this, each of the heater designs presented in this thesis are discussed.

Chapter 4 presents the experimental results of our fabricated devices, including passive microdisk transmission measurements and resonance tuning measurements. The performance of each of the heater designs is then discussed and they are compared with each other.

Chapter 5 concludes the thesis with a summary of the research performed over the course of this project. Suggestions for future projects based on this work are given. Finally, the skills acquired by the researcher (me) are listed.

Chapter 2

Background and Theory

This chapter discusses the background and theory behind the design of the devices presented in this thesis. The theory of the propagation of light in optical waveguides is given first followed by the theory of microdisk resonators. Finally, the thermal tuning of the resonances of microdisk resonators is discussed.

2.1 Optical modes of a waveguide

Light in an optical circuit propagates through waveguides. A waveguide is a device that guides light in an optical circuit analogous to how metal wires guide electrons in an electrical circuit. A waveguide consists of a core material surrounded by a cladding material in which the refractive index of the core is higher that that of the cladding. The waveguide guides light through the phenomenon of total internal reflection.

The propagation of light in a waveguide is governed by Maxwell's equations. The derivation begins with the two Maxwell curl equations:

$$\nabla \times \mathbf{E} = -\mu_0 \frac{\partial \mathbf{H}}{\partial t} \tag{2.1}$$

$$\nabla \times \mathbf{H} = \epsilon \frac{\partial \mathbf{E}}{\partial t} \tag{2.2}$$

where $\mathbf{E}$ = Electric field vector, $\mathbf{H}$ = Magnetic field vector, μ_0 = the permeability of free space and ϵ = the permittivity of the waveguide material.

Taking the curl of Eq. (2.1) and using the vector calculus identity:

$$\nabla \times \nabla \times \mathbf{A} = \nabla(\nabla \cdot \mathbf{A}) - \nabla^2 \mathbf{A} \tag{2.3}$$

we get the following wave equation for the electric field:

$$\nabla(\nabla \cdot E) - \nabla^2 E = -\mu_0 \frac{\partial(\nabla \times \mathbf{H})}{\partial t} = -\mu_0 \epsilon \frac{\partial^2 \mathbf{E}}{\partial t^2} \tag{2.4}$$

which combined with the fact that $\nabla \cdot \mathbf{E} = \frac{\rho}{\epsilon} = 0$, since we are considering a source free region, leads to:

$$\nabla^2 \mathbf{E} - \frac{n^2}{c^2} \frac{\partial^2 \mathbf{E}}{\partial t^2} = 0 \tag{2.5}$$

where n = refractive index of the waveguide material and c = the speed of light.

Similarly, the wave equation for the magnetic field is determined to be:

$$\nabla^2\mathbf{H} - \frac{n^2}{c^2}\frac{\partial^2\mathbf{H}}{\partial t^2} = 0 \tag{2.6}$$

Consider monochromatic wave solutions to Eqs. (2.5) and (2.6) of the form $\mathbf{E} = \mathbf{E}(x, y, z)e^{i\omega t}$ and $\mathbf{H} = \mathbf{H}(x, y, z)e^{i\omega t}$. Substituting these solutions into Eqs. (2.5) and (2.6) respectively, we obtain the Helmholtz equations for the electric and magnetic fields:

$$\nabla^2\mathbf{E} + n^2k_0^2\mathbf{E} = 0 \tag{2.7}$$

$$\nabla^2\mathbf{H} + n^2k_0^2\mathbf{H} = 0 \tag{2.8}$$

where $k_0 \equiv \frac{\omega}{c}$.

For waves travelling in, say, the positive z-direction, we can apply the paraxial approximation and further simplify the problem by considering solutions of the form $\mathbf{E}(x, y, z) = \mathbf{E}(x, y)e^{i\beta z}$ and $\mathbf{H}(x, y, z) = \mathbf{H}(x, y)e^{i\beta z}$. Substituting these solutions into Eqs. (2.7) and (2.8), we get:

$$\frac{\partial^2\mathbf{E}}{\partial x^2} + \frac{\partial^2\mathbf{E}}{\partial y^2} + (n^2k_0^2 - \beta^2)\mathbf{E} = 0 \tag{2.9}$$

$$\frac{\partial^2\mathbf{H}}{\partial x^2} + \frac{\partial^2\mathbf{H}}{\partial y^2} + (n^2k_0^2 - \beta^2)\mathbf{H} = 0 \tag{2.10}$$

where β = propagation constant.

The solutions to Eqs. (2.9) and (2.10) are called electromagnetic modes. We need to solve these equations and apply boundary conditions determined by the geometry of the waveguide to obtain the allowed electromagnetic modes of the waveguide. To obtain modes consistent with the law of conservation of energy, we need to apply the additional constraint that the amount of energy carried by the mode is finite.

From Eqs. (2.9) and (2.10), it appears that we have to solve 6 equations (one for each of the 3 components of **E** and **H**). However, these 6 equations are not independent. The various components of **E** and **H** are related to each other by Maxwell's equations. There are only 2 electromagnetic components that need to be solved and the rest can be obtained from Maxwell's equations. An example of this is shown in the following derivation of the modes of a planar waveguide.

2.2 Optical modes of a planar slab waveguide

One of the simplest waveguide structures is the planar slab waveguide. Consider the structure shown in Figure 2.1. The structure extends infinitely in the y-direction. The slabs of refractive index n_2 are semi-infinite in the x-direction. The modes can be sorted into two categories based on their field profiles: transverse electric (TE) modes and transverse magnetic (TM) modes.

For TE modes, the component of the electric field in the direction of propagation, E_z, is 0. Since the structure is infinite in the y-direction, the field does not vary in the y-direction i.e. all derivatives of the field components with respect

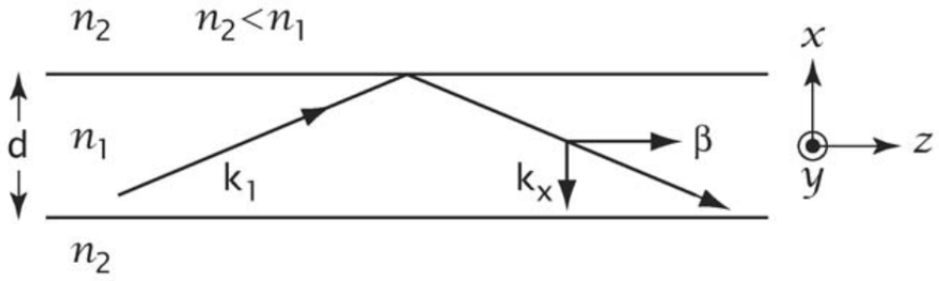

FIGURE 2.1: Structure of a planar slab waveguide. Adapted from [27].

to y are 0. Combined with Maxwell's curl equations, this reduces the number of non-zero field components from six to three: E_y, H_x and H_z. These components are related by the following equations:

$$H_x = \frac{\beta}{\omega\mu_0} E_y \tag{2.11}$$

$$H_z = \frac{-i}{\omega\mu_0} \frac{\partial E_y}{\partial x} \tag{2.12}$$

Therefore, solving for E_y from Eq. (2.9) will completely determine the electromagnetic mode profile. Eq. (2.9) needs to be solved in the core and cladding regions of the waveguide. The equation for E_y is:

$$\frac{\partial^2 E_y}{\partial x^2} + (n_i^2 k_0^2 - \beta^2) E_y = 0 \tag{2.13}$$

where $n_i, i = 1, 2$, is the refractive index of the core and cladding region respectively.

If $(n_i^2 k_0^2 - \beta^2) > 0$, the solution to Eq. (2.13) is a sinusoidal function. If $(n_i^2 k_0^2 - \beta^2) < 0$, the solution to Eq. (2.13) is an exponential function. According to the electromagnetic boundary conditions, E_y and $\frac{\partial E_y}{\partial x}$ must be continuous at the interface between the core and cladding layers. The amount of energy carried by a mode must be finite. Therefore, the field cannot increase unbounded in any part of the waveguide. Furthermore, since we are interested in guided modes, the mode energy must be confined and cannot leak out as it travels along the waveguide. These conditions, considered together, imply that the field profile in the core must be a sinusoidal function and the field profile in the cladding regions must be decaying exponential functions. The field profiles of TE modes are shown in Figure 2.2.

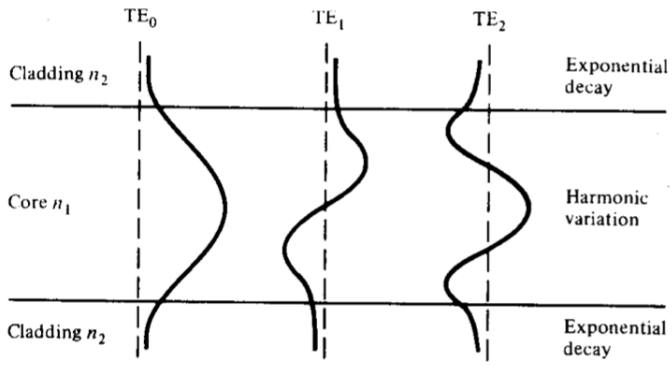

FIGURE 2.2: TE mode profiles in a planar slab waveguide. Adapted from [28].

The derivation of the TM modes is similar to that of the TE modes. In the case of the TM modes, the magnetic field component in the direction of propagation, H_z, is 0. The non-zero field components are H_y, E_x and E_z. E_x and E_z can be

expressed in terms of H_y using Maxwell's curl equations. Solving for H_y using Eq. (2.10) completely determines the mode profile.

The value of the propagation constant, β, can be determined by applying electromagnetic boundary conditions to the mode profiles shown in Figure 2.2. However, we can obtain the propagation constant using an intuitive ray optics approach. According to the ray optics formulation, light travels down the waveguide core by bouncing back and forth between the cladding layers through the phenomenon of total internal reflection, as shown in Figure 2.1.

When a ray of light encounters an interface between two mediums, the angle of incidence is related to the angle of refraction by Snell's law:

$$\sin\theta_1 = \frac{n_2}{n_1}\sin\theta_2 \tag{2.14}$$

where θ_1 = angle of incidence, θ_2 = angle of refraction and $n_{1,2}$ = refractive index in mediums 1 and 2 respectively. If $n_1 > n_2$, then $\theta_1 < \theta_2$. The angle of incidence, θ_1, for which the angle of refraction, θ_2, becomes 90° is called the critical angle.

$$\theta_{crit} = \sin^{-1}\frac{n_2}{n_1} \tag{2.15}$$

For angles of incidence greater than θ_{crit}, the light ray is completely reflected at the interface. This phenomenon is known as total internal reflection.

Light rays being guided by a waveguide must not leak out as they propagate along the waveguide. Hence, the light rays must be incident onto the core-cladding interfaces at an incidence angle greater than the critical angle. Furthermore, for guided modes, the phase shift experienced by the light wave in one round-trip between the two core-cladding interfaces must be an integer multiple of 2π. The round-trip phase shift consists of the phase accumulated through propagation and the phase shift due to reflection at each interface. The phase accumulated through propagation can be expressed as:

$$\phi_{prop} = 2dn_1k_0\cos\theta_m \tag{2.16}$$

where d = thickness of waveguide core and θ_m = incidence angle of the m_{th} mode.

The phase shift due to reflection is given by the Fresnel equations. The phase shift experienced by TE polarised light incident at an angle greater than the critical angle is given by:

$$\phi_{TE} = -2\tan^{-1}\left(\frac{\sqrt{n_1^2\sin^2\theta - n_2^2}}{n_1\cos\theta}\right) \tag{2.17}$$

Therefore, the round-trip phase shift experienced by the light must be:

$$2dn_1k_0\cos\theta_m + 2\phi_{TE}[\theta_m] = m2\pi \tag{2.18}$$

where $m = 0, 1, 2, \ldots$

For each value of m, Eq. (2.18) can be solved for θ_m. The propagation constant corresponding to each value of θ_m is given by:

$$\beta_m = n_1 k_0 \sin\theta_m \tag{2.19}$$

Thus, a discrete set of propagation constants, β_m, are obtained with each corresponding to a mode of the waveguide. However, Eq. (2.18) does not yield valid solutions for θ_m for all values of m. For a given set of n_1, n_2 and d, there exists a cutoff value for m above which the values of θ_m obtained from Eq. (2.18) becomes less than the critical angle. These modes are not supported by the waveguide. Hence, the number of allowed modes of a waveguide is finite. The number of allowed modes of a waveguide is determined by the thickness of the core, with higher thicknesses supporting a higher number of modes.

A frequent requirement for photonic devices is that the waveguides must be single mode i.e. the waveguides only support the fundamental ($m = 0$) mode. This requires that the thickness of the waveguide core be limited so as to only support the $m = 0$ mode. This thickness can be determined by determining the smallest core thickness for which the $m = 1$ mode is supported. This can be determined from Eq. (2.18) by setting $m = 1$ and $\theta_m = \theta_{crit}$. For a silicon-on-insulator (SOI) waveguide, $n_1 \approx 3.5, n_2 \approx 1.45$ and $\theta_{crit} \approx 24.47°$. Plugging in these values into Eq. (2.18), we obtain a core waveguide thickness of ≈ 243 nm for 1550 nm wavelength light. Therefore, waveguides with core thickness less than

243 nm will not support the $m = 1$ mode and hence, the waveguide will be single mode. This is the reason why many SOI photonics foundries implement a silicon slab thickness of 220 nm.

2.3 Optical modes of complex waveguide geometries

The planar slab waveguide, while simple to analytically solve, is not very useful since it only confines light in one direction. Three dimensional waveguide structures such as strip waveguides, as shown in Figure 2.3, and rib waveguides, as shown in Figure 2.4, confine light in two directions and are the most commonly used waveguide structures in practical photonic devices.

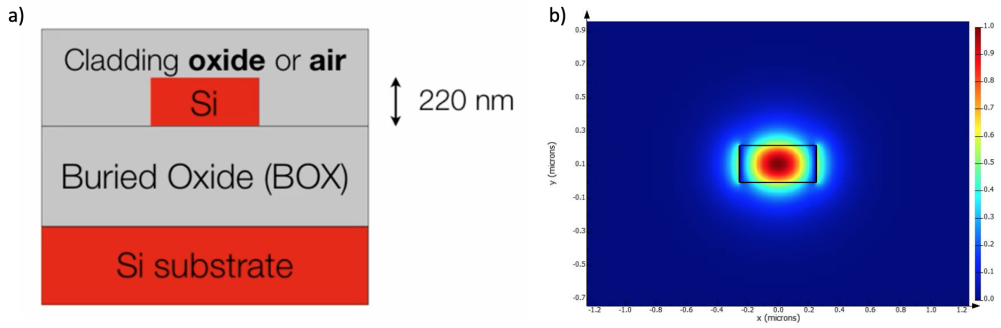

FIGURE 2.3: a) Structure of a SOI strip waveguide and b) the electric field profile of its fundamental mode

The electromagnetic modes of strip and rib waveguides can be obtained by solving Eqs. (2.9) and (2.10), similar to the solution to the planar slab waveguide. However, since the geometry is more complex, analytical solutions are very difficult to obtain (for many geometries, analytical solutions don't exist). Marcatili's method and the effective index method are two approximate analytical techniques

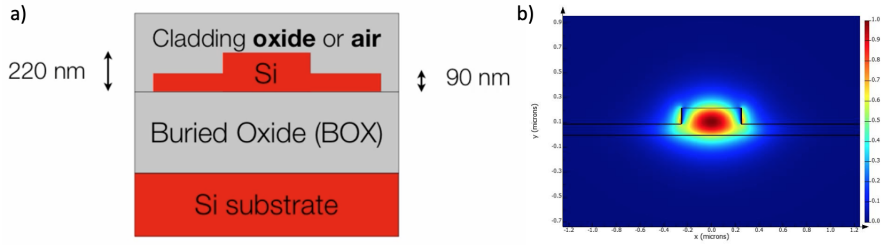

FIGURE 2.4: a) Structure of a SOI rib waveguide and b) the electric field profile of its fundamental mode

that obtain solutions for such waveguide structures by making certain simplifying assumptions. Using numerical techniques such as the Finite Difference Eigenmode method implemented in simulation software packages such as Lumerical Mode is a powerful method to obtain the mode profiles and their respective propagation constants for complex waveguide geometries.

2.4 Microdisk resonators

Traveling wave resonators (TWR), such as microrings and microdisks, are important and versatile photonic devices. TWR's function by trapping and concentrating light within them. They can be used in constructing laser cavities, generating true time delay, as optical filters, in sensing applications etc.

A microdisk resonator, as shown in Figure 2.5, is a type of TWR. A TWR is a waveguiding structure that supports modes that travel in a closed path and interfere with themselves. In the case of a microdisk resonator, the supported modes are called whispering gallery modes that travel along the edge of the microdisk.

In order for light to constructively interfere with itself, it's wavelength must fit a whole number of times in the optical path length of the TWR. Therefore, the

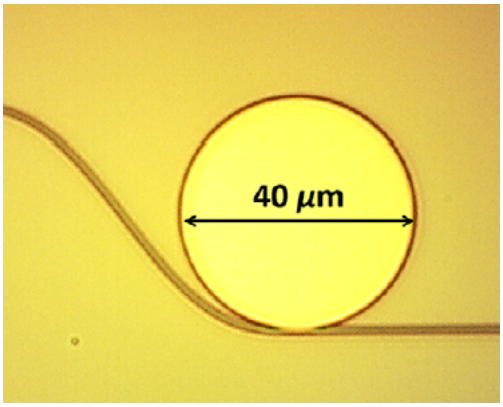

FIGURE 2.5: A microdisk resonator coupled to a bus waveguide. Adapted from [9].

resonance condition for a microdisk resonator is:

$$\lambda_{res} = \frac{n_{eff} L}{m} = \frac{2\pi R n_{eff}}{m} \tag{2.20}$$

where n_{eff} = effective index of the microdisk mode, L = optical path length of the microdisk, R = radius of the microdisk and $m = 1, 2, 3, \ldots$

The spacing between successive resonances is called the free spectral range (FSR) and is given by:

$$FSR = \frac{\lambda^2}{n_g L} = \frac{\lambda^2}{2\pi R n_g} \tag{2.21}$$

where n_g = group index of the microdisk mode.

The microdisk needs to interact with the outside world for it to be useful. This can be accomplished by placing it near a bus waveguide. The interaction between

the resonator and the bus waveguide can be modeled by the following equations [29]:

$$\frac{da}{dt} = (j\omega_0 - \frac{1}{\tau_0} - \frac{1}{\tau_c})a + \kappa S_{in} \tag{2.22}$$

$$S_{out} = S_{in} - \kappa^* a \tag{2.23}$$

where a = amplitude of the resonator mode field, ω_0 = resonance angular frequency of the resonator, κ = coupling coefficient between the bus waveguide mode and the resonator mode, S_{in} = amplitude of the bus waveguide mode before interacting with the resonator and S_{out} = amplitude of the bus waveguide mode after interacting with the resonator. τ_0 is the time constant of the rate of energy loss due to the various loss mechanisms of the resonator such as bending loss and scattering loss due to sidewall roughness. It is called the intrinsic time constant. τ_c is the time constant of the rate at which energy is coupled out of the resonator mode and into the bus waveguide mode. It is called the coupling or extrinsic time constant.

Solving Eq. (2.22) in the frequency domain i.e. setting $a = a(\omega)e^{j\omega t}$, we obtain expressions for the amplitude of the resonator mode field and the transmission as a function of frequency:

$$a(\omega) = \frac{\kappa}{j(\omega - \omega_0) + \frac{1}{\tau_0} + \frac{1}{\tau_c}} S_{in}(\omega) \tag{2.24}$$

$$T(\omega) = \frac{S_{out}(\omega)}{S_{in}(\omega)} = \frac{j(\omega - \omega_0) + \frac{1}{\tau_0} - \frac{1}{\tau_c}}{j(\omega - \omega_0) + \frac{1}{\tau_0} + \frac{1}{\tau_c}} \tag{2.25}$$

We define the intrinsic quality factor of the resonator as $Q_0 = \frac{\omega_0 \tau_0}{2}$. Similarly, we define the coupling or extrinsic quality factor of the resonator as $Q_c = \frac{\omega_0 \tau_0}{2}$. Substituting these expressions into Eq. (2.25), we get [29]:

$$T(\omega) = \frac{S_{out}(\omega)}{S_{in}(\omega)} = \frac{\frac{2j(\omega-\omega_0)}{\omega_0} + \frac{1}{Q_0} - \frac{1}{Q_c}}{\frac{2j(\omega-\omega_0)}{\omega_0} + \frac{1}{Q_0} + \frac{1}{Q_c}} \tag{2.26}$$

Eq. (2.26) is used in this thesis to extract the intrinsic and extrinsic Q-factors of microdisk resonators. This is done by fitting Eq. (2.26) to dips in the transmission data in different wavelength regimes. The loaded Q-factor is the combination of the intrinsic and extrinsic Q-factors and is what can be obtained directly from the transmission measurement. It is given by the equations:

$$\frac{1}{Q_L} = \frac{1}{Q_0} + \frac{1}{Q_e} \tag{2.27}$$

$$Q_L = \frac{\lambda_{res}}{FWHM} \tag{2.28}$$

where Q_l = loaded Q-factor and FWHM = full width half maximum of the resonance.

There are three coupling regimes that a microdisk resonator can be in. They are characterized by the relative value of Q_0 and Q_c. When $Q_0 < Q_c$, the resonator

is said to be undercoupled. This is because a high Q_c implies a low coupling coefficient between the resonator and the bus waveguide. When $Q_0 > Q_c$, the resonator is said to be overcoupled since a low Q_c implies a high coupling coefficient between the resonator and the bus waveguide. When $Q_0 = Q_c$, the resonator is said to be critically coupled. From Eq. (2.26), it can be seen that the transmission at resonance drops to 0 when the resonator is critically coupled. When extracting the Q-factors from Eq. (2.26), it is important to know which coupling regime the resonator is in. This can be obtained by measuring the phase change in the transmission or by setting the coupling regime beforehand while designing the resonator.

The value of the coupling coefficient, κ, can be calculated using coupled mode theory. It is given by the following expression [29]:

$$\kappa = \frac{-j\omega_0}{2} \frac{\int dz dA \Delta(n^2) e_r^* e_W e^{j(m\phi - \beta z)}}{\sqrt{n_r^2 n_W^2} \sqrt{v_g V_m A_m}} \tag{2.29}$$

There are three main terms in this expression that determine the strength of the coupling. The first is the interaction length of the resonator and waveguide, represented by the integration volume $dzdA$. The larger the integration volume, the stronger the coupling. The second is the overlap of the waveguide mode and resonator mode field profiles represented by the term $e_r^* e_W$. The greater the field overlap, the stronger the coupling. This is mainly determined by the gap between the resonator and the bus waveguide. The final factor is the level of phase mismatch between the waveguide mode and the resonator mode, represented by the term $(m\phi - \beta z)$. Phase mismatch refers to the difference in effective index between

the resonator mode and the waveguide mode. The greater the phase mismatch, the weaker the coupling. Phase mismatch is often the most important factor in determining the coupling since a small phase mismatch can amplify its effect over the interaction length and drastically reduce the coupling. Hence, when designing resonators, it is important to have good phase matching between the bus waveguide mode and the desired resonator mode to couple into.

2.5 Thermal tuning of microdisk resonances

The refractive index of materials, such as silicon, changes with temperature due to the thermo-optic effect. The change in refractive index per unit of temperature change is defined as the thermo-optic coefficient. For instance, the thermo-optic coefficient of silicon at 300 K at a wavelength of 1550 nm is, $\frac{dn}{dT} = 1.8 \times 10^{-4} K^{-1}$. This property allows us to tune the speed at which light travels in a waveguide by changing its temperature. The integration of this functionality with microdisk resonators is extremely useful. The resonance wavelength of a microdisk resonator, given by Eq. (2.20), depends on the effective index of the disk mode. By changing the refractive index of the mode by heating the microdisk, we can change its resonance wavelength. This can be used to design tunable lasers, modulators, tunable true time delay, tunable filters etc. Controlled heating can be achieved by introducing resistive heater structures alongside the microdisk resonators.

The amount of phase change caused by the heater is given by [26]:

$$\Delta\phi = \frac{2\pi}{\lambda}\left(\frac{dn_{eff}}{dT}\right)\Delta T L \tag{2.30}$$

where n_{eff} = effective index of the microdisk mode, ΔT = change in temperature of the light guiding structure and L = length of the light guiding structure that is heated (in this case, the portion of the edge of the microdisk that is heated).

The amount of temperature change of the light guiding structure is determined by its mass and the fraction of the heater power that reaches it and is given by:

$$\Delta T = \frac{\eta P}{C \rho V} \tag{2.31}$$

where P = the applied power to the heater, η = efficiency of heater in resonance tuning, C = heat capacity of the heated material, ρ = density of the heated material and V = volume of the heated material.

The determination of the volume of the heated material is not straightforward. From the heat maps that are simulated in the design chapter, we shall see that the microdisk structure is not heated uniformly. Since the microdisk mode exists very close to the edge of the microdisk, only the temperature change of the edge of the disk matters. Furthermore, there are three different materials in the light guiding structure explored in this thesis that are being heated. They are the silicon microdisk, the SiO_2 bottom cladding and the TeO_2 top cladding, each having a different density, specific heat capacity and mode overlap. In order to simplify the problem, we absorb these constants into the efficiency as follows:

$$\Delta T = \eta P \tag{2.32}$$

The units of η are Kelvin/Watt (or Kelvin/mW). η signifies the average temperature change of the light guiding structure overlapping with the mode per unit of applied heater power. A higher value of η means that the temperature of the light guiding structure (in this case, the disk edge and the immediately surrounding cladding material) increases more per unit of applied heater power. Since a higher temperature change means a higher phase change, a higher value of η signifies a greater heater efficiency.

Inserting Eq. (2.32) into Eq. (2.30), the phase change caused by the heater is given by:

$$\Delta\phi = \frac{2\pi}{\lambda}\left(\frac{dn_{eff}}{dT}\right)\eta PL \tag{2.33}$$

Therefore, the efficiency is given by:

$$\eta = \frac{\Delta\phi\lambda}{2\pi\left(\frac{dn_{eff}}{dT}\right)PL} \tag{2.34}$$

The phase change for a microdisk resonator is given by:

$$\Delta\phi = 2\pi\left(\frac{\Delta\lambda_{res}}{FSR}\right) \tag{2.35}$$

where $\Delta\lambda_{res}$ = shift in the resonance wavelength due to heating and FSR = free spectral range.

The FSR can be obtained from the transmission data or calculated from Eq. (2.21). Therefore, the efficiency of the heater is given by:

$$\eta = \frac{\Delta\lambda_{res}\lambda}{\left(\frac{dn_{eff}}{dT}\right) PL \times FSR} \tag{2.36}$$

In this thesis, we design thermally tuned silicon microdisk resonators. Several designs for the heater structure are proposed. Eq. (2.36) is used to compare their tuning efficiencies.

Chapter 3

Fabrication and Design

This chapter begins with a description of the fabrication process that was used in fabricating the devices presented in this thesis. This is followed by a detailed description of the design of each device.

3.1 Advanced Micro Foundry (AMF) platform

The devices investigated in this thesis were fabricated via Advanced Micro Foundry (AMF) located in Singapore. AMF offers a full active silicon-on-insulator platform that provides various functionalities. It has three possible silicon waveguide layer thicknesses of 220 nm, 150 nm and 90 nm based on a 220 nm thick silicon layer on a 2 μm thick buried oxide layer on a silicon substrate. It incorporates many active functionalities such as doped silicon layers with various doping levels, heaters and germanium photodetectors. These layers are embedded in a 3 µm thick silicon dioxide layer that serves as the top cladding for the silicon waveguides. Figure 3.1 shows a cross-sectional schematic of the features of the AMF platform that are relevant to our designs.

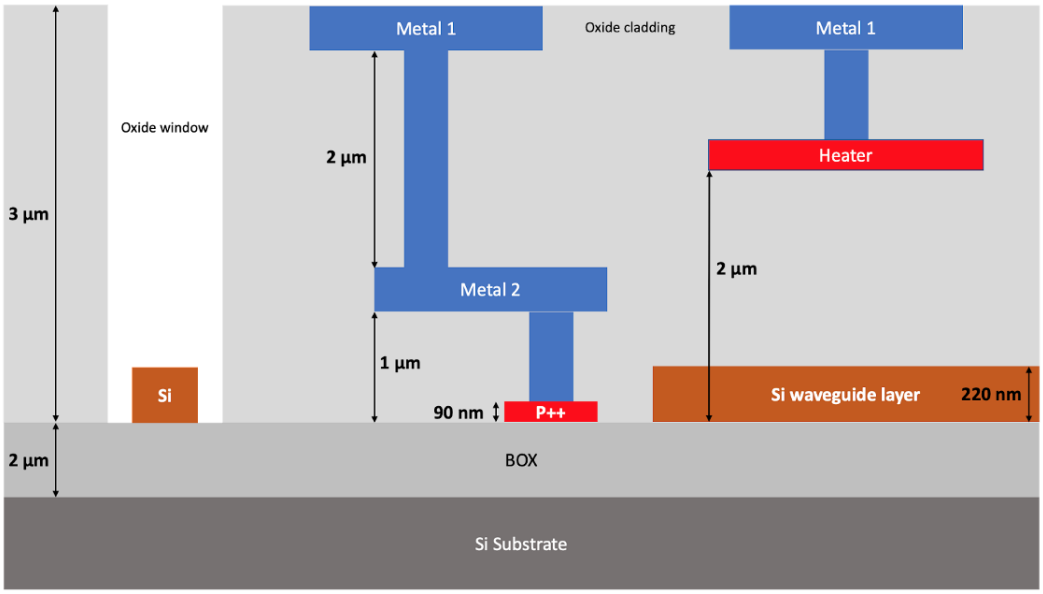

FIGURE 3.1: Cross-sectional schematic of the AMF platform

AMF uses 193 nm or 248 nm UV lithography to define the silicon layer. The minimum feature size for the main 220 nm silicon layer is 180 nm. The heater layer is made of titanium nitride (TiN) and is embedded in the foundry oxide 2 μm above the silicon layer. It is 100 nm thick and has a minimum feature size of 2 μm. AMF offers the capability to create a window in the SiO_2 foundry cladding to expose the silicon devices underneath. This feature is used extensively in the devices designed in this thesis for the purpose of depositing a tellurium dioxide cladding. Once the devices are fabricated on the wafer, deep trenches are etched for edge coupling and the wafer is diced into chips and shipped to our lab for post-processing.

3.2 Deposition of tellurium dioxide cladding

Once the chips are received from AMF, tellurium dioxide is deposited on them. This causes the devices that have the oxide window to be cladded by TeO_2. The TeO_2 film is deposited using radio frequency magnetron reactive sputtering [12]. Reactive sputtering has many attractive qualities as a technique for creating thin films, especially for the devices studied in this thesis. It is a simple one step procedure that is employed in research as well as commercial settings. It can be performed at low temperature which is important for samples containing active components. The deposition rates can be as high as 25 nm/min which enables the deposition of films upto 350 nm thick in less than 15 minutes. A highly pure metallic tellurium target is used as the source. Argon gas is used to bombard the target and sputter tellurium atoms towards the sample. Oxygen gas is introduced into the chamber to react with the sputtered tellurium atoms to form tellurium dioxide that then deposits onto the sample. Previous studies have shown that, to create low loss films, the ideal ratio of tellurium to oxygen in the film is 2:1 [13, 30, 31]. This is achieved through careful control of the oxygen flow rate, argon flow rate and the sputtering power. For our devices, we deposit a TeO_2 film that is 350 nm thick and has a measured refractive index of 2.13. The thickness and refractive index measurement is done using spectroscopic ellipsometry.

3.3 Tunable TeO_2-Si microdisk resonator design considerations

In this thesis, we design tunable silicon microdisk resonators. In most heater designs, the heater is positioned above the edges of the microdisk to enable efficient and uniform heating as shown in Figure 3.2. However, in our designs, we require that the foundry cladding above the microdisk be removed to enable the deposition of our TeO_2 cladding. Since the heater layers provided by AMF are embedded in the foundry cladding, the heater cannot be placed directly above the microdisk. The purpose of the heater designs in this thesis is to investigate efficient heater structures for tunable microdisk resonators that are compatible with our requirement of a TeO_2 cladding for our devices.

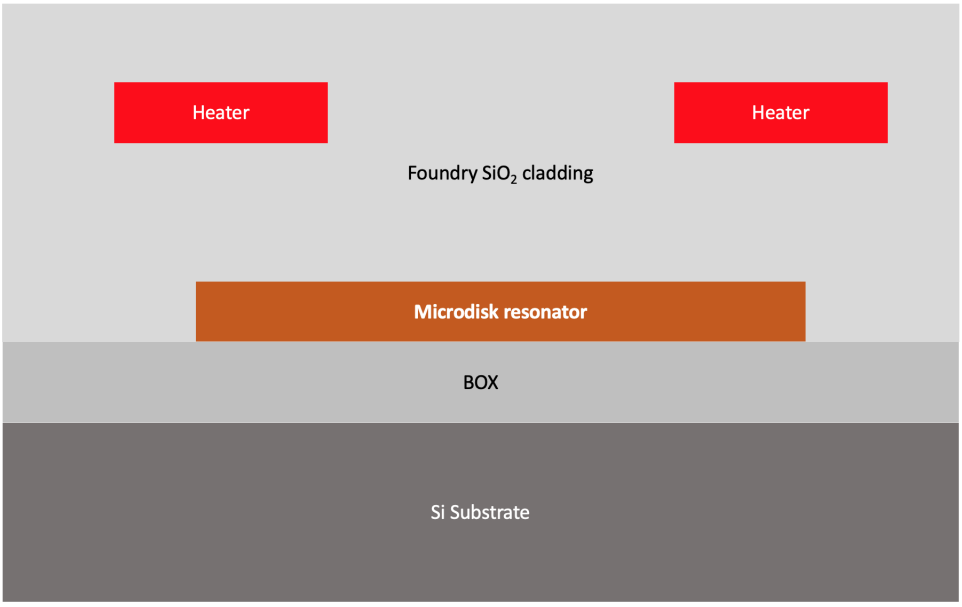

FIGURE 3.2: Silicon microdisk resonator with heater for resonance tuning

3.4 Finite difference eigenmode solver simulations

We use the finite difference eigenmode solver in Lumerical MODE to design and characterize the thermally tuned microdisk resonators in this thesis. The finite difference method is a numerical technique for solving partial differential equations such as Maxwell's equations. We use Lumerical MODE to solve for the modes of the microdisk, extract the effective index of those modes and determine the thermo-optic coefficients of those modes.

Figure 3.3 and Figure 3.4 show cross-sectional schematics of the simulation region setup in Lumerical MODE that is used to solve for the modes of our devices. The simulation region contains half the cross section of the microdisk. The microdisk is simulated by using the curved waveguide feature in Lumerical MODE and setting the centre of the curved waveguide to the left border of the simulation region. The radius of the microdisk was set to 25 µm. The thickness of the TeO_2 cladding was set to 350 nm. The thickness of the silicon microdisk and silicon slab were set to 220 nm and 90 nm respectively, in accordance with the AMF foundry process. The simulations were performed at a wavelength of 1550 nm.

Material	Thermo-optic coefficient $\left(\frac{dn}{dT}\right)$
Silicon	1.8×10^{-4} [26]
SiO_2	9.6×10^{-6} [32]
TeO_2	2.3×10^{-5} [33]

TABLE 3.1: Thermo-optic coefficients of the materials in the device structure

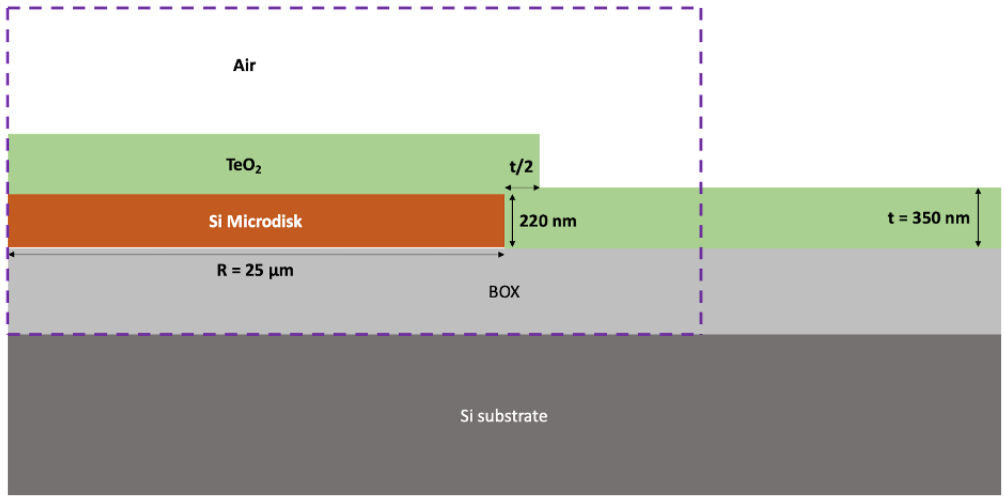

FIGURE 3.3: Cross-sectional schematic of the simulation region for the strip disk

Table 3.1 lists the thermo-optic coefficients of silicon, silicon dioxide and tellurium dioxide. The thermo-optic coefficients of the fundamental TE mode of the microdisk resonators were calculated by simulating the effective index of the devices at various temperatures and calculating the slope. Since silicon has the highest thermo-optic coefficient that is an order of magnitude larger than the next highest, which is TeO_2, the largest contribution to the thermo-optic coefficient of the microdisk mode is expected to come from silicon. The contributions from the thermo-optic coefficients of TeO_2 and SiO_2 are expected to be much smaller. However, in some heater designs, very little heat reaches the microdisk and the silicon does not get heated much. In this case, the thermo-optic coefficient of the microdisk mode is mainly determined by the thermo-optic coefficients of the cladding materials. Therefore, thermo-optic coefficient calculations were performed assuming either only the silicon was heated, only the cladding was heated or both the silicon and the cladding was heated. The effective index of a strip disk as shown

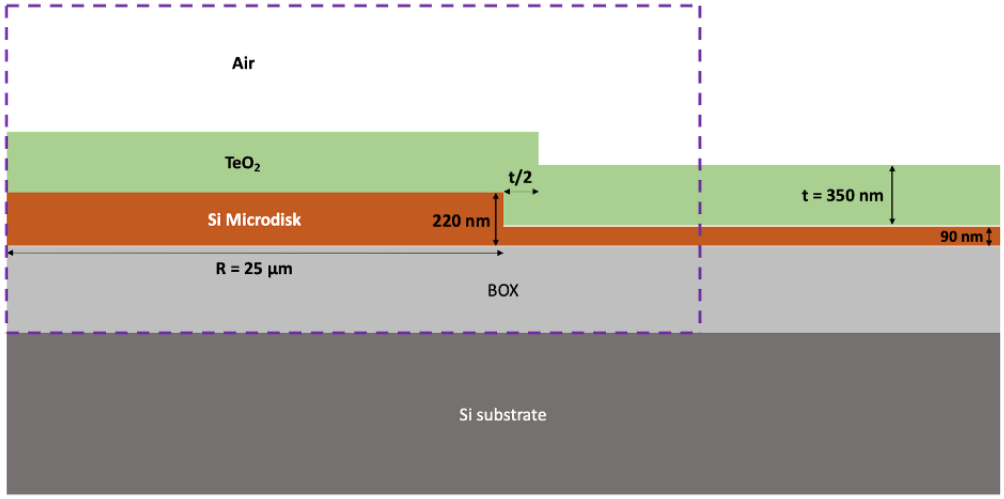

FIGURE 3.4: Cross-sectional schematic of the simulation region for the ridge disk

in Figure 3.3 was simulated to be $n_{eff} = 2.780$. The effective index of a ridge disk as shown in Figure 3.4 was simulated to be $n_{eff} = 2.785$. Table 3.2 lists the thermo-optic coefficients of the 1st TE mode for strip disks and ridge disks subjected to the different heating conditions at a wavelength of 1550 nm. Figure 3.5 shows a sample effective index vs temperature graph from which the thermo-optic coefficient is extracted from the slope of the graph.

Microdisk device + heating condition	Effective thermo-optic coefficient $\left(\frac{dn}{dT}\right)$
Strip disk + only Si heated	1.71×10^{-4}
Strip disk + only cladding heated	2.80×10^{-6}
Strip disk + both Si and cladding heated	1.74×10^{-4}
Ridge disk + only Si heated	1.71×10^{-4}
Ridge disk + only cladding heated	2.80×10^{-6}
Ridge disk + both Si and cladding heated	1.74×10^{-4}

TABLE 3.2: Effective thermo-optic coefficients of devices under different heating conditions

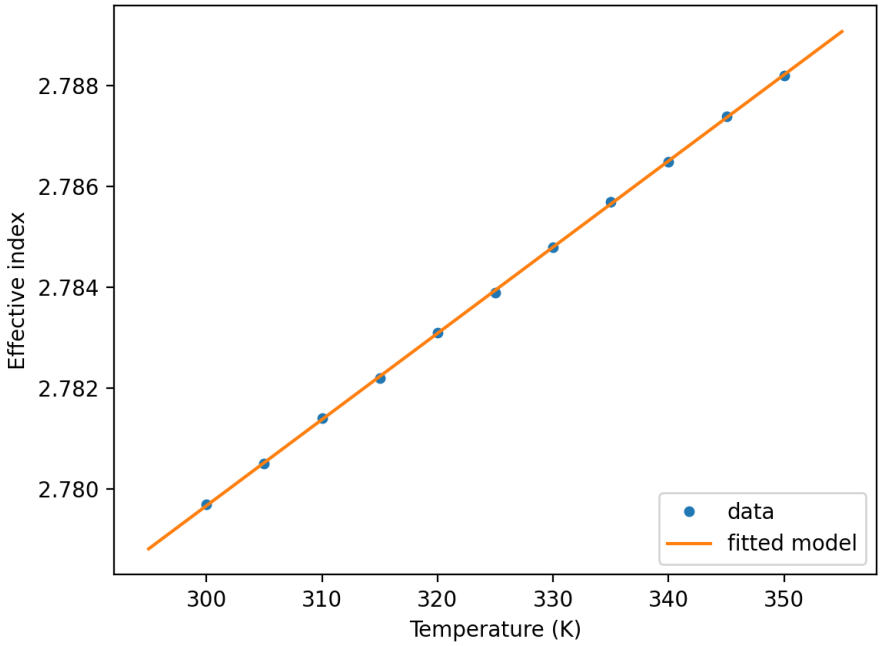

FIGURE 3.5: Effective index vs temperature graph for a strip disk of radius 25 μm with only the silicon heated

3.5 Heater designs

In this thesis, we have designed 5 different heater structures and evaluated their performance in resonance tuning. We have designed 2 types of heaters: silicon heaters and titanium nitride (TiN) heaters. In the silicon heater designs, heating is achieved by passing electric current through a strip of doped silicon positioned near the microdisk resonator. In the TiN heater designs, heating is achieved by passing electric current through a strip of TiN positioned near the microdisk resonator. The details of each design are presented below.

3.5.1 Silicon heater design 1

Figures 3.6, 3.7 and 3.8 illustrate the structure of the silicon heater design 1. The foundry oxide above the microdisk and bus waveguide have been removed. The distance between the silicon microdisk and bus waveguide from the foundry oxide is set to be 5 μm to allow enough space for the TeO_2 cladding. The P++ layer is positioned so as to be as close to the microdisk as possible while also not interfering with the disk mode. 4 μm was selected as a safe distance from the disk, but in future this distance might be reduced. Once this device is received from AMF, we deposit a 300-400 nm thick TeO_2 film on top that fills the space above the microdisk and bus waveguide.

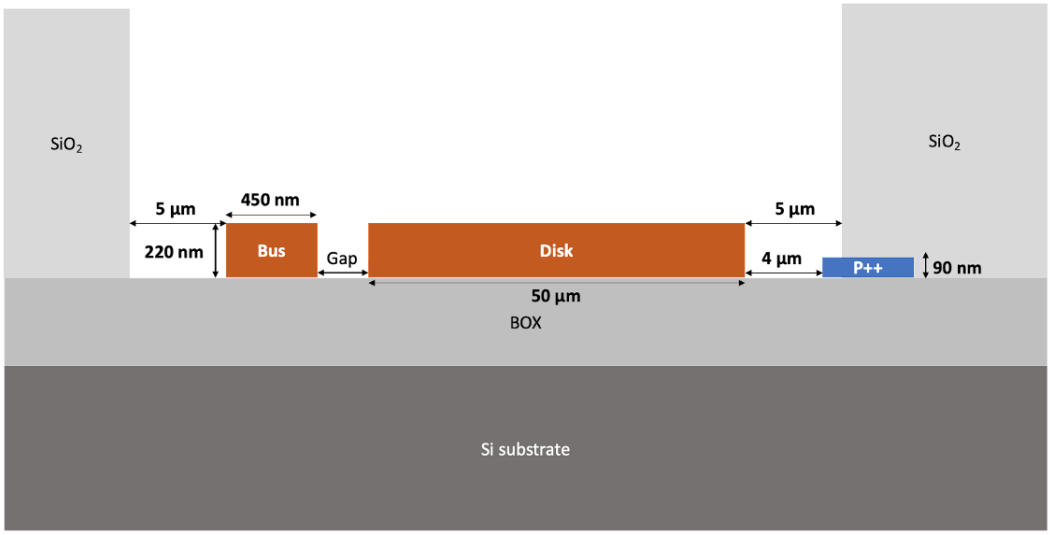

FIGURE 3.6: Cross-sectional schematic of Silicon heater design 1. Heating is achieved by passing electric current through the P++ strip. The oxide above the microdisk has been removed. We deposit TeO_2 on the chips as a cladding for the microdisk.

In this design, heating is achieved by passing electric current through the P++ strip. When electric current is passed through the P++ strip, it heats up due to Joule heating. The heat is then conducted sideways through the TeO_2 cladding

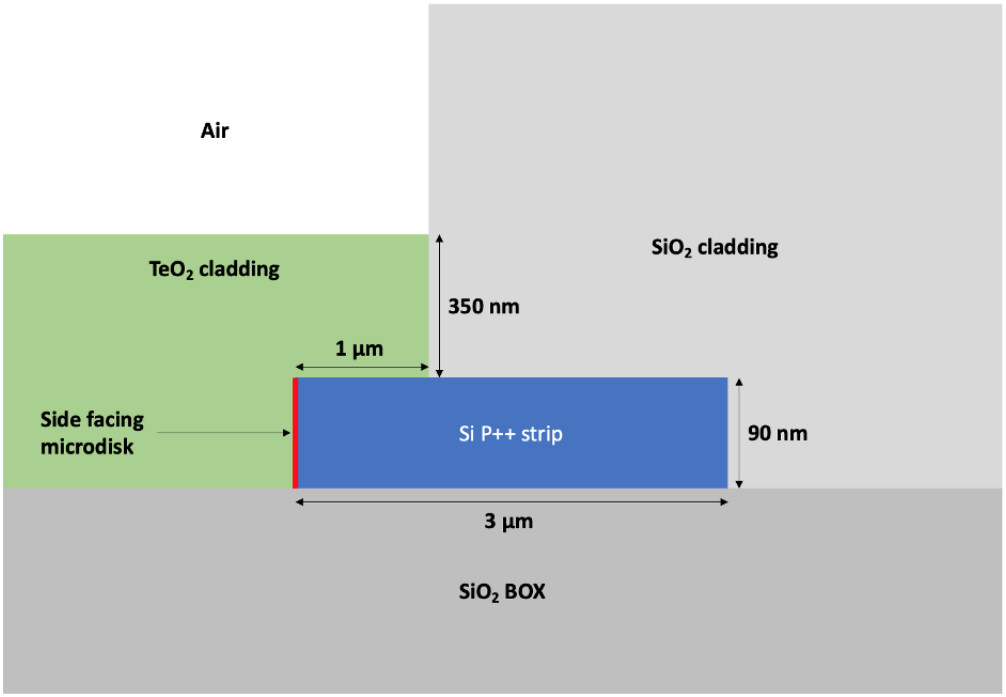

FIGURE 3.7: Heater strip and its surroundings in Si heater design 1

and into the disk. As we can observe from the simulated temperature distributions in Figures 3.9 and 3.10, very little heat from the heater reaches the disk. This can be attributed to a couple of factors. The first is that TeO_2 is a poor conductor of heat with a thermal conductivity of about 2 W m^{-1} K^{-1} [34]. The second is that the surface area of the heater strip in the direction facing the microdisk is a small fraction of its total surface area. The one-dimensional form of Fourier's law of heat conduction is given by:

$$q = -k\frac{dT}{dx} \tag{3.1}$$

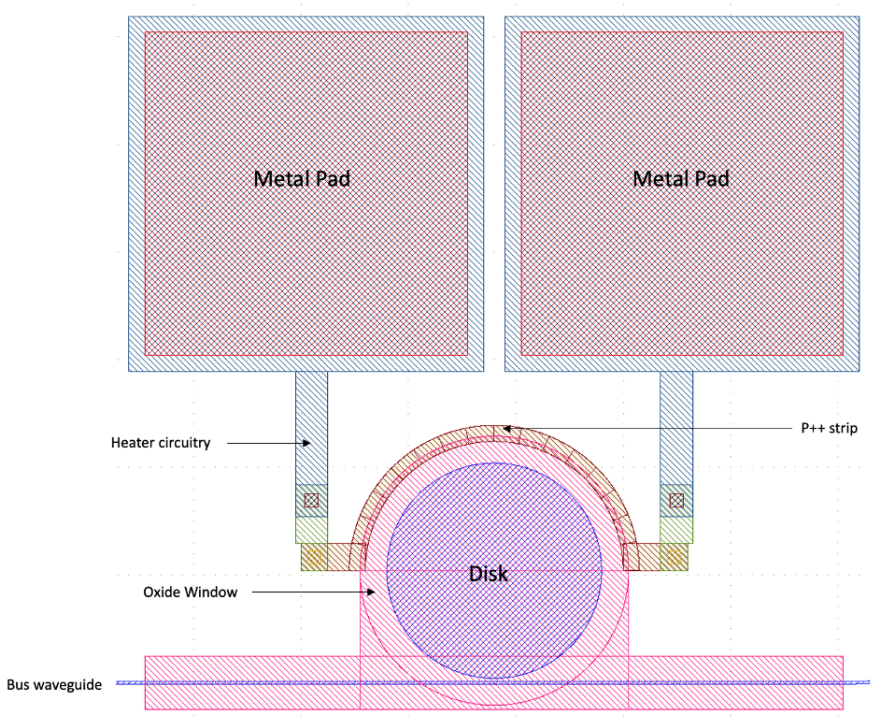

FIGURE 3.8: Top view schematic of Silicon heater design 1

where q = heat flux density (W/m^2) and k = material thermal conductivity (W m^{-1} K^{-1}).

The thermal conductivity of TeO_2 is $k_1 = 2$ W m^{-1} K^{-1} and the thermal conductivity of SiO_2 is $k_2 = 1.38$ W m^{-1} K^{-1} [35]. We can estimate the temperature gradient in each of the four directions using the heatmap. The estimated temperature gradients are: in the upward direction, $\frac{dT}{dx} \approx -16.67$, in the left and right directions, $\frac{dT}{dx} \approx -50$ and in the downward direction, $\frac{dT}{dx} \approx -100$. Using Fourier's law, we can estimate an upper limit for the efficiency of the heater i.e. the ratio of the heater power directed towards the disk to the total heater power. The thermal power flowing in each direction is given by:

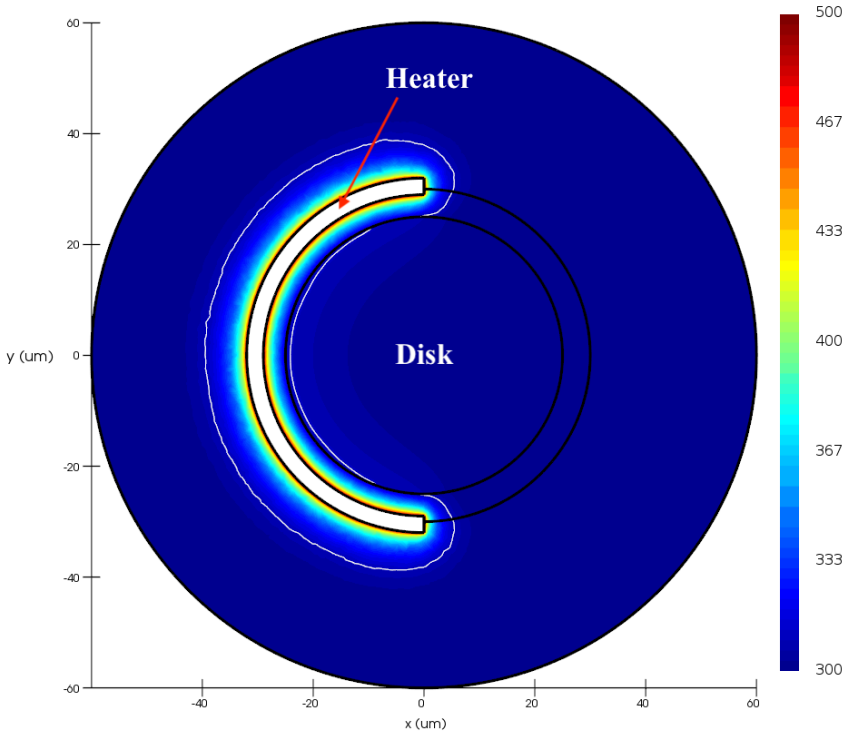

FIGURE 3.9: Top view of the simulated temperature distribution for silicon heater design 1. The doped silicon strip has been set to a temperature of 500 K. The white contour line indicates a temperature of 310 K.

In the upward direction,

$$
\begin{aligned}
P_{up} &= q_{up} A_{up} \\
&= \left[-k_1 A_{TeO_2} \left(\frac{dT}{dx} \right)_{up} \right] + \left[-k_2 A_{SiO_2} \left(\frac{dT}{dx} \right)_{up} \right] \\
&= \left\{ \left[-2 \left(\frac{\pi(30^2 - 29^2)}{2} \right) (-16.67) \right] + \left[-1.38 \left(\frac{\pi(32^2 - 30^2)}{2} \right) (-16.67) \right] \right\} \times 10^{-12} \\
&= 7.57 \times 10^{-9} W
\end{aligned}
\tag{3.2}
$$

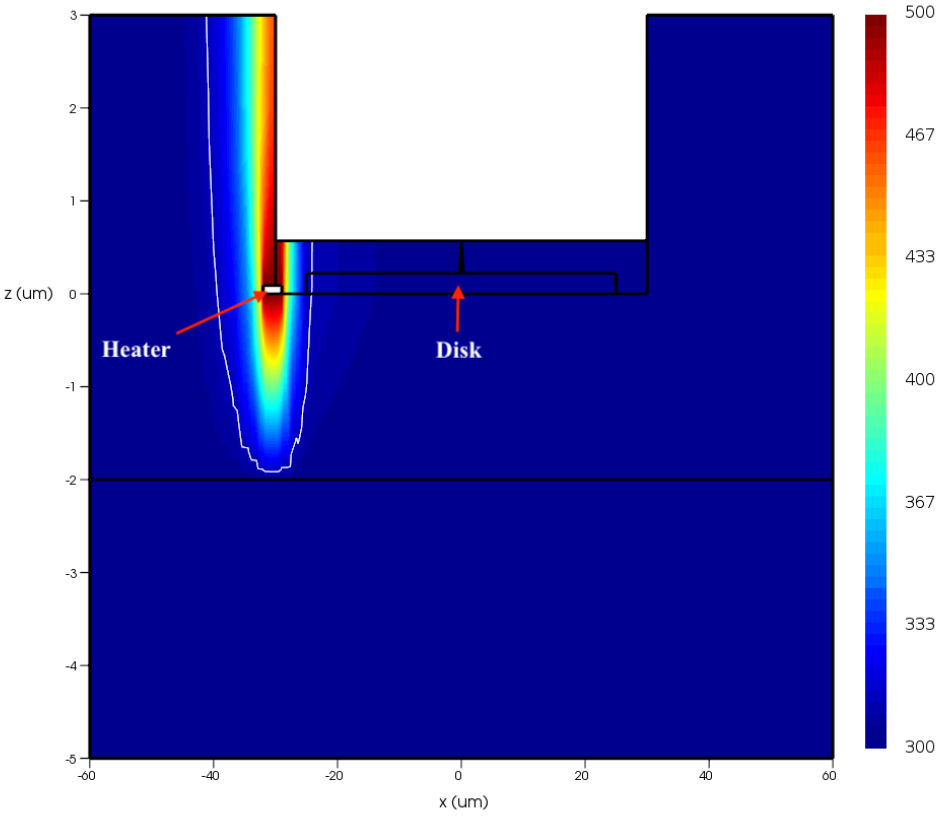

FIGURE 3.10: Cross-sectional view of the simulated temperature distribution for silicon heater design 1. The doped silicon strip has been set to a temperature of 500 K. The white contour line indicates a temperature of 310 K.

In the left direction,

$$\begin{aligned} P_{left} &= q_{left} A_{left} \\ &= -k_1 A \left(\frac{dT}{dx}\right)_{left} \\ &= [(-2)(\pi)(29)(0.09)(-50)] \times 10^{-12} \\ &= 8.20 \times 10^{-10} W \end{aligned} \tag{3.3}$$

In the downward direction,

$$\begin{aligned} P_{down} &= q_{down} A_{down} \\ &= -k_2 A \left(\frac{dT}{dx}\right)_{down} \\ &= \left[(-1.38)\left(\frac{\pi(32^2 - 29^2)}{2}\right)(-100)\right] \times 10^{-12} \\ &= 3.97 \times 10^{-8} W \end{aligned} \tag{3.4}$$

In the right direction,

$$\begin{aligned} P_{right} &= q_{right} A_{right} \\ &= -k_2 A \left(\frac{dT}{dx}\right)_{right} \\ &= [(-1.38)(\pi)(32)(0.09)(-50)] \times 10^{-12} \\ &= 6.24 \times 10^{-10} W \end{aligned} \tag{3.5}$$

In the above calculations, we are using a disk radius of 25 µm. The factor of 10^{-12} is the conversion factor from μ^2 to m^2.

Therefore, the estimated efficiency of the heater is given by:

$$\tau = \frac{P_{left}}{P_{total}} = \frac{P_{left}}{P_{up} + P_{left} + P_{down} + P_{right}} = 0.017 = 1.7\% \tag{3.6}$$

The above estimated efficiency of 1.7 % is an upper limit since the above calculations make some simplifying assumptions. It is assumed that heat flows in only 4 directions i.e. up, down, left and right whereas in reality, heat flows in every direction with each direction having a different temperature gradient. Therefore, the actual efficiency of this heater design is expected to be lower than this value.

3.5.2 Silicon heater design 2

Figures 3.11, 3.12 and 3.13 illustrate the structure of the silicon heater design 2. This design is similar to design 1 except that the microdisk and bus waveguide are ridge structures instead of strip structures. The microdisk is connected to the heating strip by the silicon slab layer. Heating is achieved by passing electric current through the P++ strip, which heats up due to Joule heating. However, in this design, the heat is conducted into the disk through the 90 nm silicon slab as compared to the previous design, in which the heat was conducted through the TeO_2 cladding. The thermal conductivity of silicon is 149 W m^{-1} K^{-1} [26] whereas the thermal conductivity of TeO_2 is 2 W m^{-1} K^{-1}. Hence, the heat conduction through the silicon slab is much more efficient than compared to the TeO_2 cladding. Therefore, this heater design is expected to be more efficient at resonance tuning than compared to design 1.

We can estimate the efficiency of this heater design using Fourier's law, similar to the calculations performed for silicon heater design 1. The temperature gradients surrounding the heater strip can be estimated from the heatmaps in Figures 3.14 and 3.15 as follows: in the upward direction, $\frac{dT}{dx} \approx -16.67$, in the left direction, $\frac{dT}{dx} \approx -26.46$, in the right direction, $\frac{dT}{dx} \approx -37.50$ and in the downward

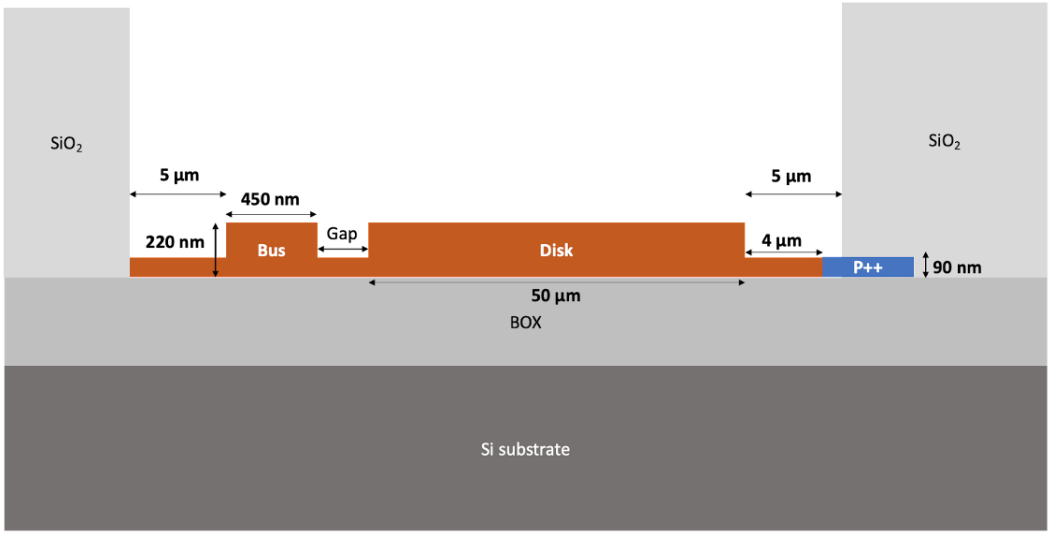

FIGURE 3.11: Cross-sectional schematic of Silicon heater design 2. Heating is achieved by passing electric current through the P++ strip. The oxide above the microdisk has been removed. We deposit TeO_2 on the chips as a cladding for the microdisk.

direction, $\frac{dT}{dx} \approx -100$. The thermal power flowing in each direction is given by:

In the upward direction,

$$\begin{aligned} P_{up} &= q_{up} A_{up} \\ &= \left[-k_1 A_{TeO_2} \left(\frac{dT}{dx} \right)_{up} \right] + \left[-k_2 A_{SiO_2} \left(\frac{dT}{dx} \right)_{up} \right] \\ &= \left\{ \left[-2 \left(\frac{\pi(30^2 - 29^2)}{2} \right) (-16.67) \right] + \left[-1.38 \left(\frac{\pi(32^2 - 30^2)}{2} \right) (-16.67) \right] \right\} \times 10^{-12} \\ &= 7.57 \times 10^{-9} W \end{aligned} \tag{3.7}$$

In the left direction,

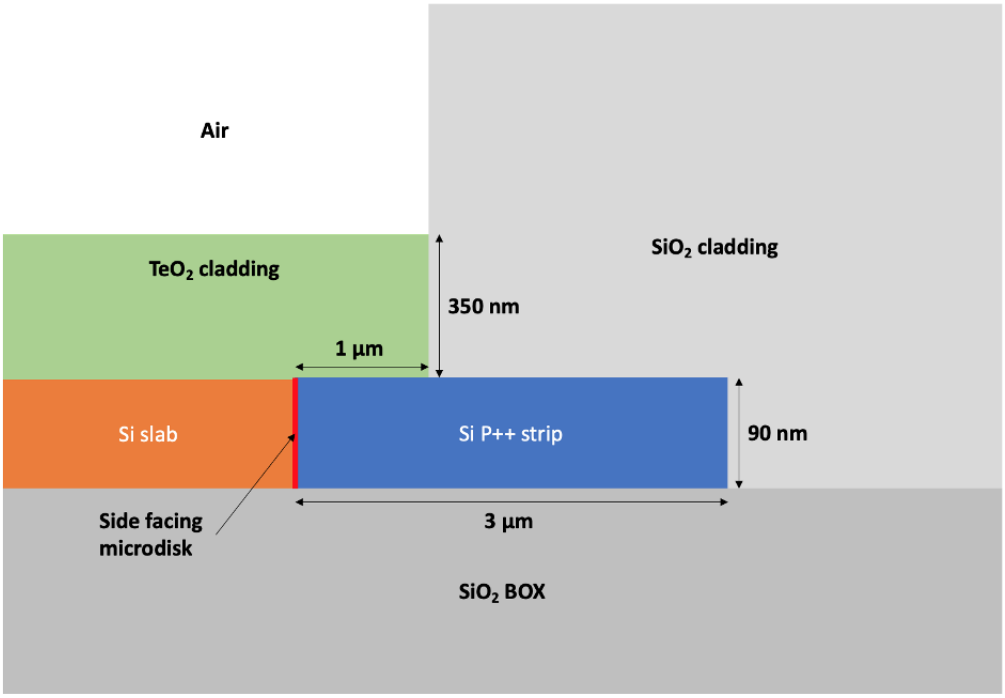

FIGURE 3.12: Heater strip and its surroundings in Si heater design 2

$$\begin{aligned} P_{left} &= q_{left} A_{left} \\ &= -k_3 A \left(\frac{dT}{dx}\right)_{left} \\ &= [(-149)(\pi)(29)(0.09)(-26.46)] \times 10^{-12} \\ &= 3.23 \times 10^{-8} W \end{aligned} \tag{3.8}$$

In the downward direction,

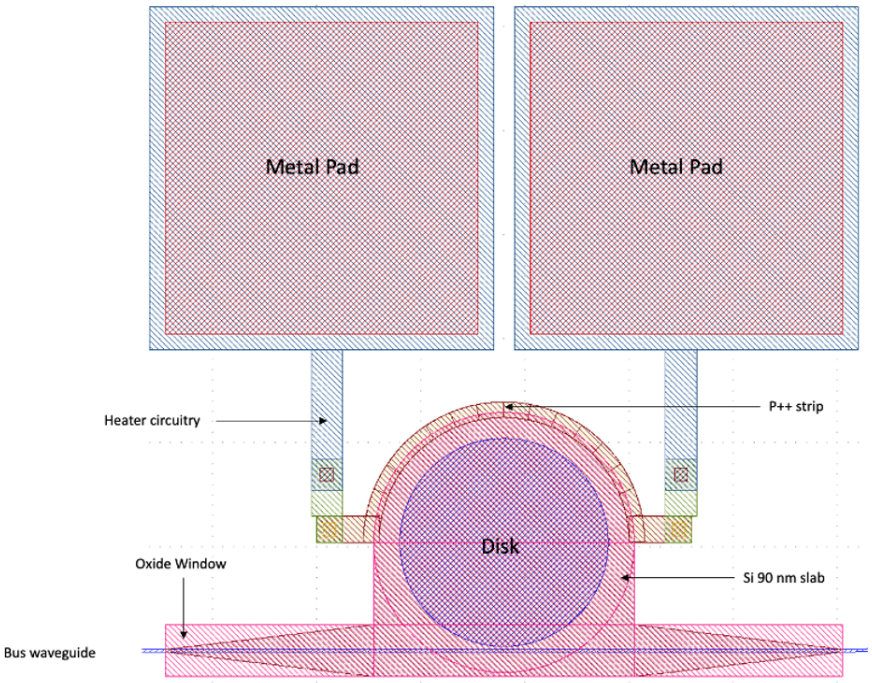

FIGURE 3.13: Top view schematic of Silicon heater design 2

$$\begin{aligned} P_{down} &= q_{down} A_{down} \\ &= -k_2 A \left(\frac{dT}{dx}\right)_{down} \\ &= \left[(-1.38)\left(\frac{\pi(32^2 - 29^2)}{2}\right)(-100)\right] \times 10^{-12} \\ &= 3.97 \times 10^{-8} W \end{aligned} \tag{3.9}$$

In the right direction,

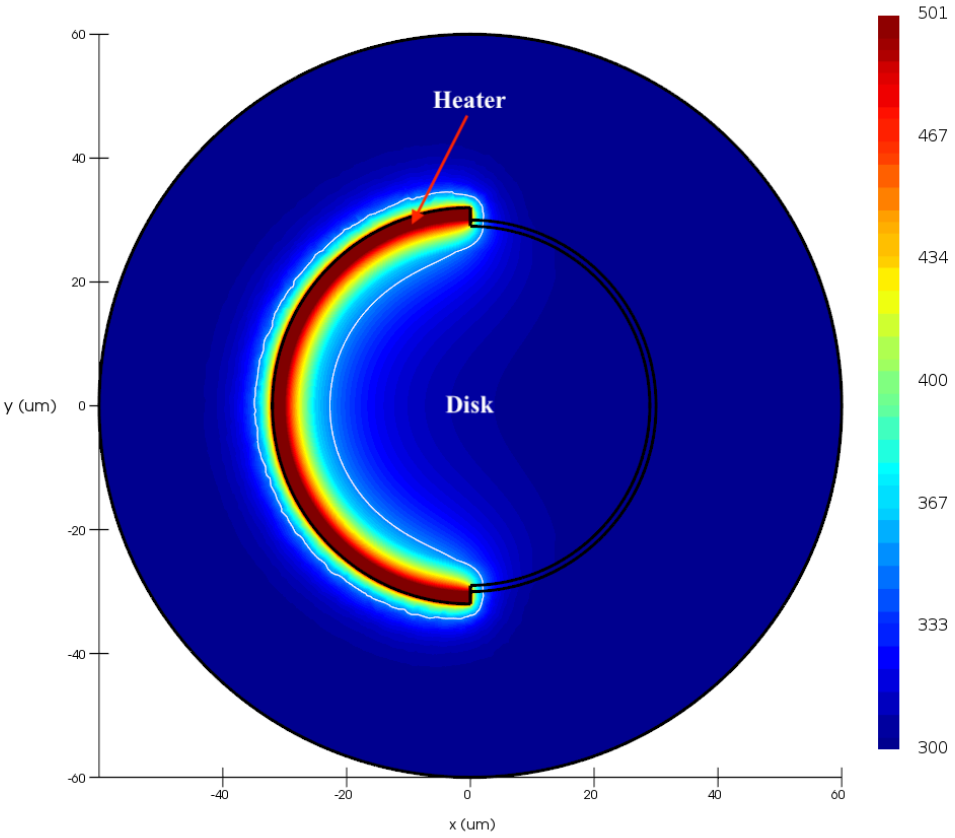

Figure 3.14: Top view of the simulated temperature distribution for silicon heater design 2. The doped silicon strip has been set to a temperature of 500 K. The white contour line indicates a temperature of 350 K.

$$\begin{aligned} P_{right} &= q_{right} A_{right} \\ &= -k_2 A \left(\frac{dT}{dx}\right)_{right} \\ &= [(-1.38)(\pi)(32)(0.09)(-37.50)] \times 10^{-12} \\ &= 4.68 \times 10^{-10} W \end{aligned} \tag{3.10}$$

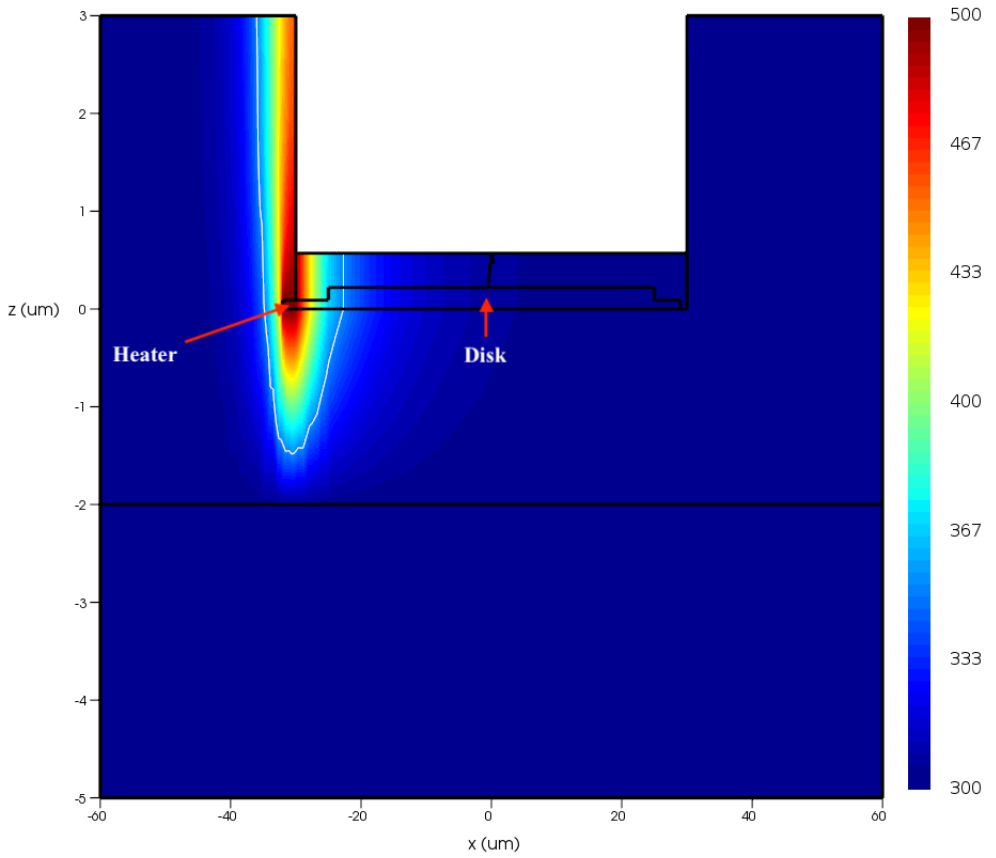

FIGURE 3.15: Cross-sectional view of the simulated temperature distribution for silicon heater design 2. The doped silicon strip has been set to a temperature of 500 K. The white contour line indicates a temperature of 350 K.

In the above calculations, k_1 is the heat conductivity of TeO_2, k_2 is the heat conductivity of SiO_2 and k_3 is the heat conductivity of Si. We are using a disk radius of 25 µm. The factor of 10^{-12} is the conversion factor from μm^2 to m^2.

Therefore, the estimated upper limit of the efficiency of the heater is given by:

$$\tau = \frac{P_{left}}{P_{total}} = \frac{P_{left}}{P_{up} + P_{left} + P_{down} + P_{right}} = 0.40 = 40\% \tag{3.11}$$

The above estimated efficiency of 40 % is much higher than the estimated efficiency of the silicon heater design 1. Although the actual efficiency of this heater design will be lower than this value, we expect it to be much higher than the silicon heater design 1.

3.5.3 TiN heater design 1

Figures 3.16 and 3.17 illustrate the structure of the TiN heater design 1. The layout of the bus waveguide and microdisk is identical to the silicon heater designs. Heating is achieved by running current through the TiN strip which heats up due to Joule heating. The heat is then conducted down through the SiO_2 cladding and across the TeO_2 cladding into the disk. The heater strip is positioned as close to the microdisk as allowed by the foundry process. The advantage of this design is avoiding the heater design influencing the microdisk mode by separating the two.

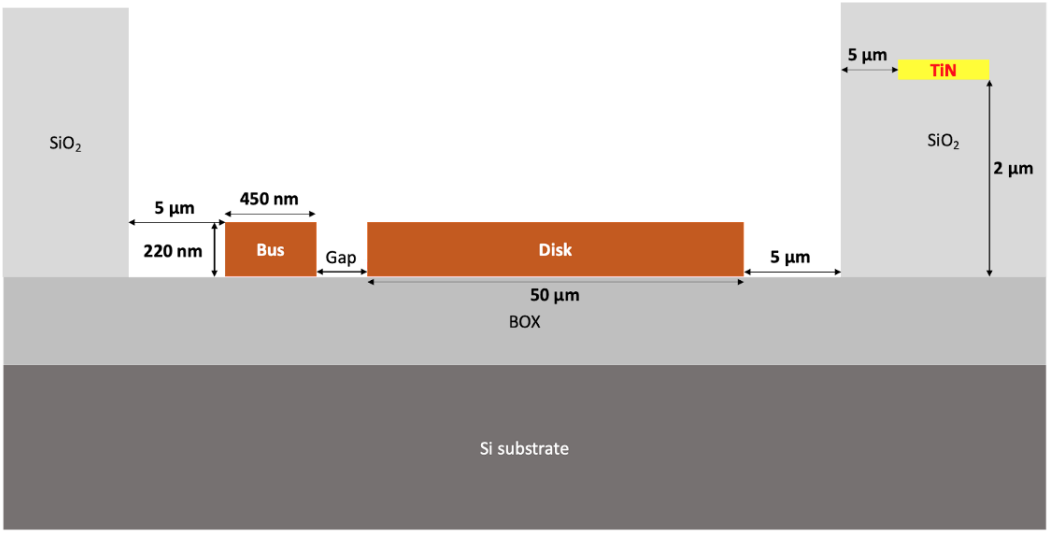

FIGURE 3.16: Cross-sectional schematic of TiN heater design 1. Heating is achieved by passing electric current through the TiN strip. The oxide above the microdisk has been removed. We deposit TeO_2 on the chips as a cladding for the microdisk.

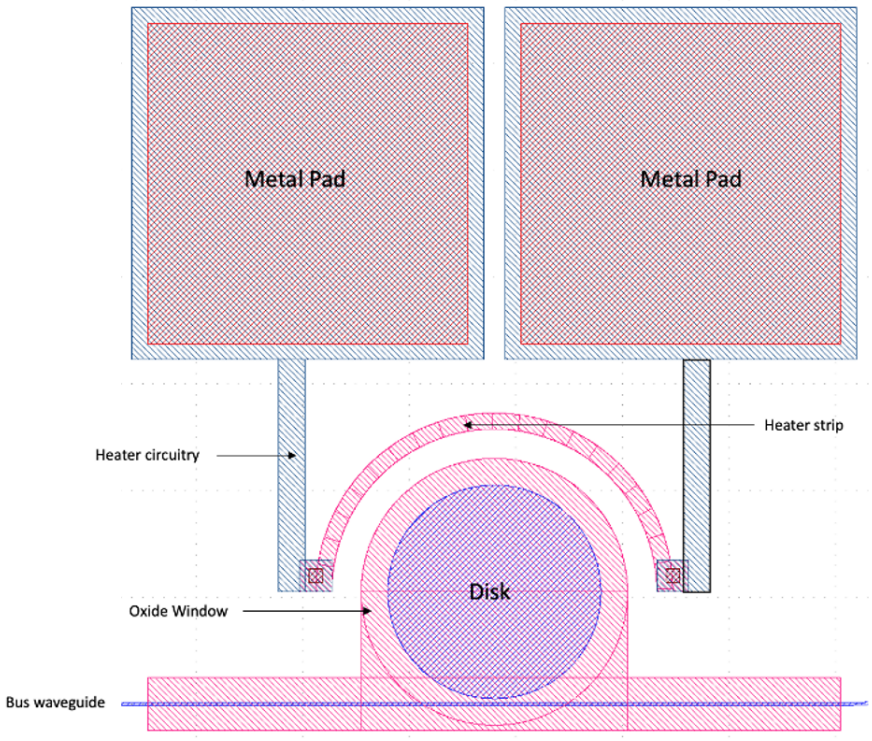

FIGURE 3.17: Top view schematic of TiN heater design 1

From the heatmaps in Figures 3.18 and 3.19, we can see that almost no heat reaches the microdisk. This can be attributed to the large distance and the lack of a straight path for the heat to be conducted from the heater to the microdisk. The temperature of the microdisk is almost unchanged whereas the temperature of the TeO_2 cladding increases slightly. Hence, in this design, the main contribution to the resonance tuning will be from the thermo-optic coefficient of TeO_2. The thermo-optic coefficient of TeO_2 is about $2.3 \times 10^{-5} K^{-1}$ which is an order of magnitude lower than the thermo-optic coefficient of silicon which is about $1.8 \times 10^{-4} K^{-1}$. Hence, the tuning efficiency of this heater design is expected to be much lower than that of the silicon heater designs.

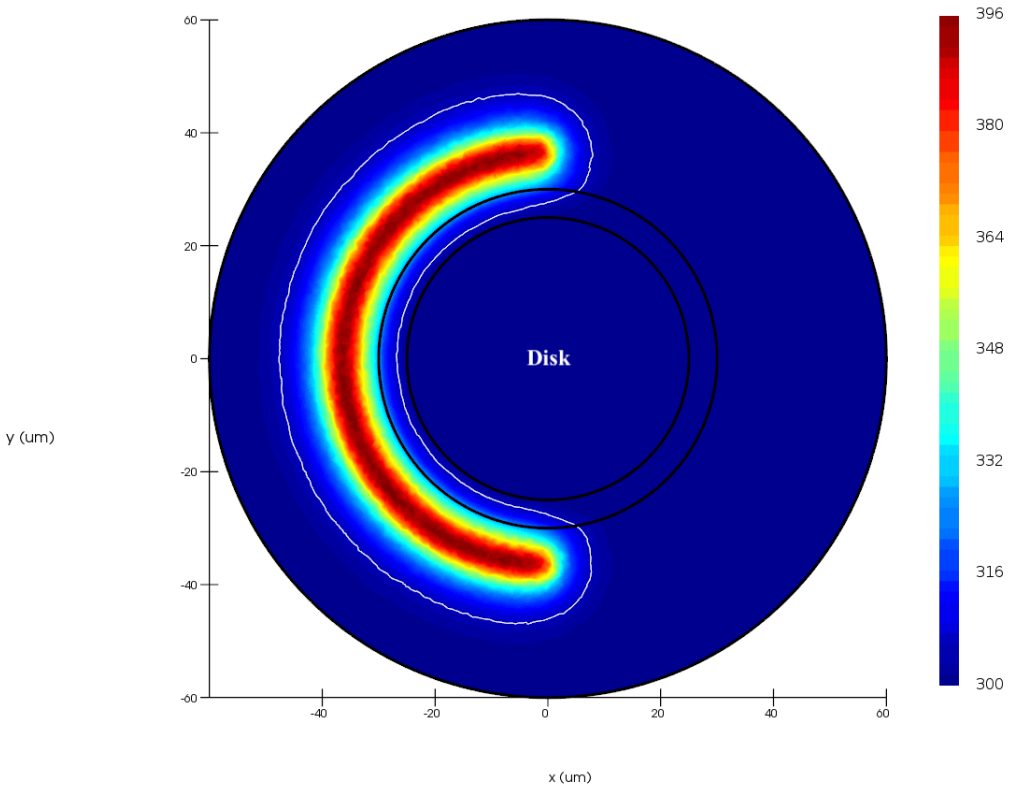

FIGURE 3.18: Top view of the simulated temperature distribution for TiN heater design 1. The TiN strip has been set to a temperature of 500 K. The white contour line indicates a temperature of 305 K.

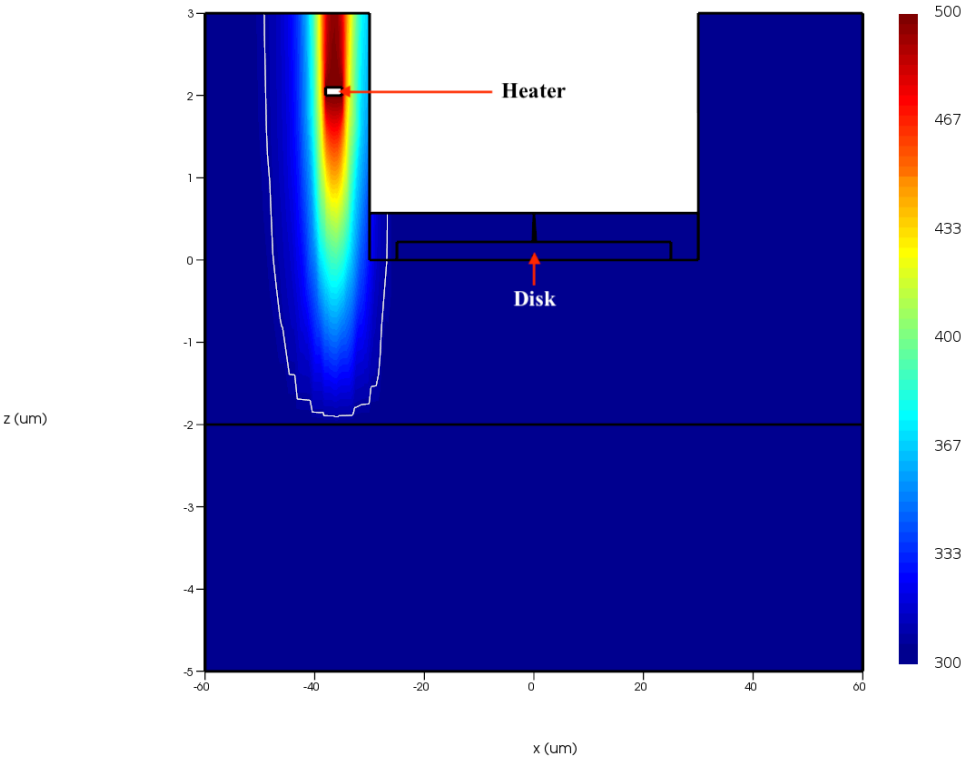

FIGURE 3.19: Cross-sectional view of the simulated temperature distribution for TiN heater design 1. The TiN strip has been set to a temperature of 500 K. The white contour line indicates a temperature of 305 K.

3.5.4 TiN heater design 2

Figures 3.20, 3.21 and 3.22 illustrate the structure of the TiN heater design 2. In heater designs in which the microdisk has the foundry cladding, the best place to position the heater is above the disk where the disk mode is located. This leads to most of the heater power reaching the disk and increases the efficiency of the heater. However, with the factory cladding removed due to the requirement for a custom cladding, this is not possible. The TiN heater design 2 is an attempt to balance the requirement for a high efficiency heater along with the requirement for a custom cladding. The oxide window is limited to the edge of the microdisk where the mode is located. This leaves the foundry oxide above the interior of the disk intact. The heater is positioned above the interior of the disk. The oxide window does not go all the way around the disk to allow the heater to be connected to the metal pads. The relative position of the heater strip and the oxide window is constrained by the foundry process which requires the heater to be positioned a minimum of 5 µm away from the oxide window. A major concern with this design is the transition between the TeO_2 cladding and the SiO_2 cladding, which occurs at two points on the disk. These transitions lead to mode-mismatch losses and reflections every time light crosses these points. Since light traveling in the disk crosses these points thousands of times, the accumulation of these losses could render the disk non-functional. To mitigate these losses, the shape of the window at the transitions has been designed to be a taper across the disk mode to make the transitions more gradual.

From the heatmaps in Figures 3.23 and 3.24, we can see that most of the heat reaches the microdisk since the heater is located directly above the disk. The disk

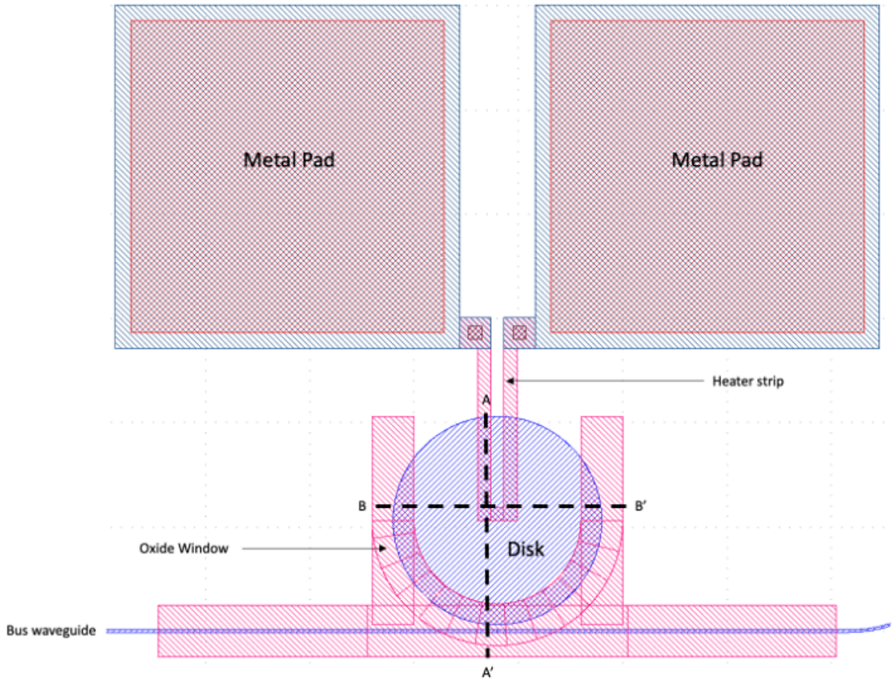

Figure 3.20: Top view schematic of TiN heater design 2. The A-A' and B-B' cross-sectional lines are shown

is not heated uniformly with some parts being heated much more than others. The contour lines in the heatmap show the varying temperatures reached at different points of the disk. The tuning efficiency of this heater is expected to be quite high since a large portion of the applied heater power reaches the disk.

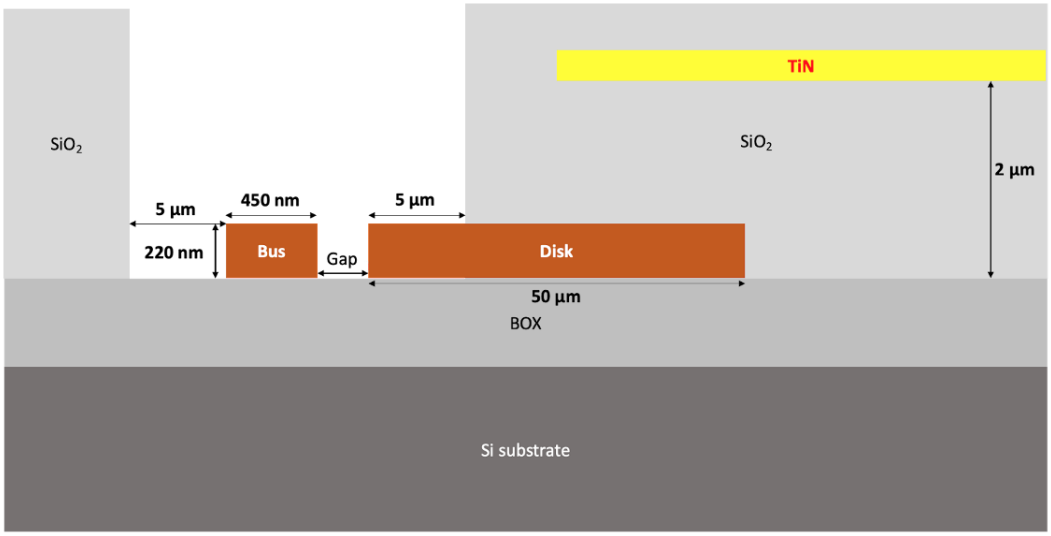

FIGURE 3.21: A-A' Cross-sectional schematic of TiN heater design 2

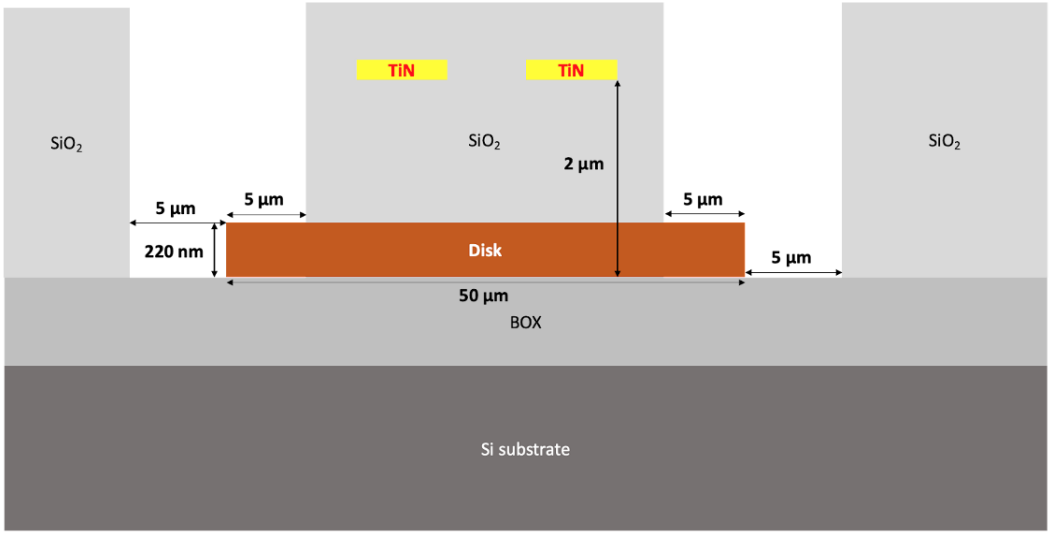

FIGURE 3.22: B-B' Cross-sectional schematic of TiN heater design 2

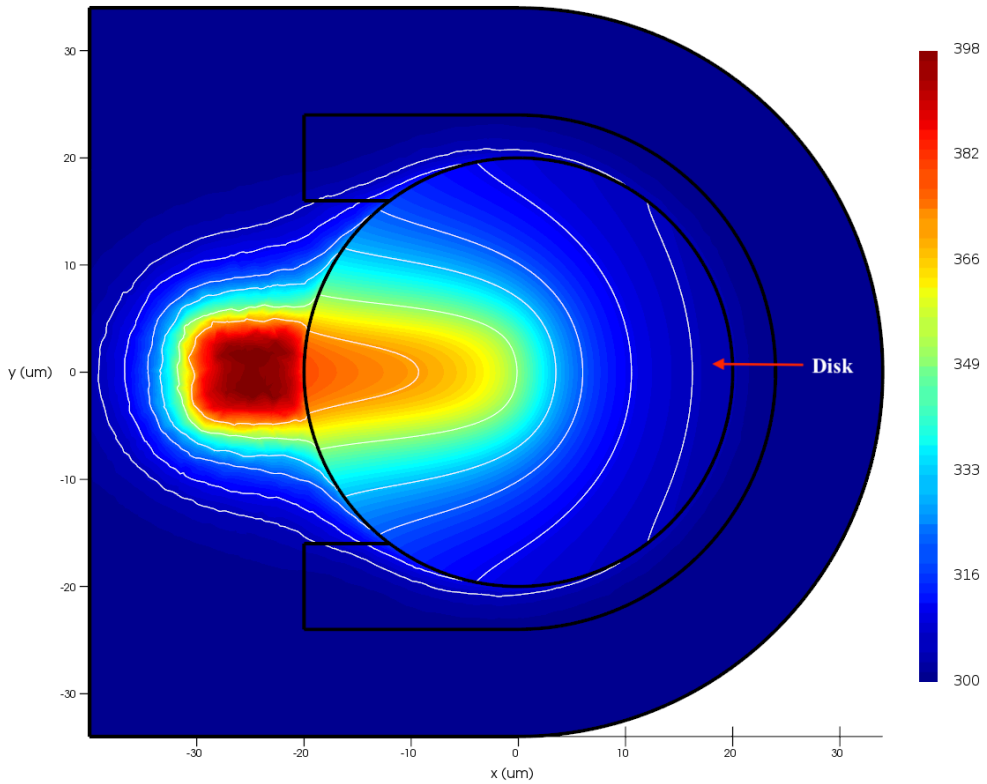

Figure 3.23: Top view of the simulated temperature distribution for TiN heater design 2. The TiN strip has been set to a temperature of 500 K. The white contour lines indicate the temperatures: 305 K, 310 K, 320 K, 330 K, 350 K and 370 K.

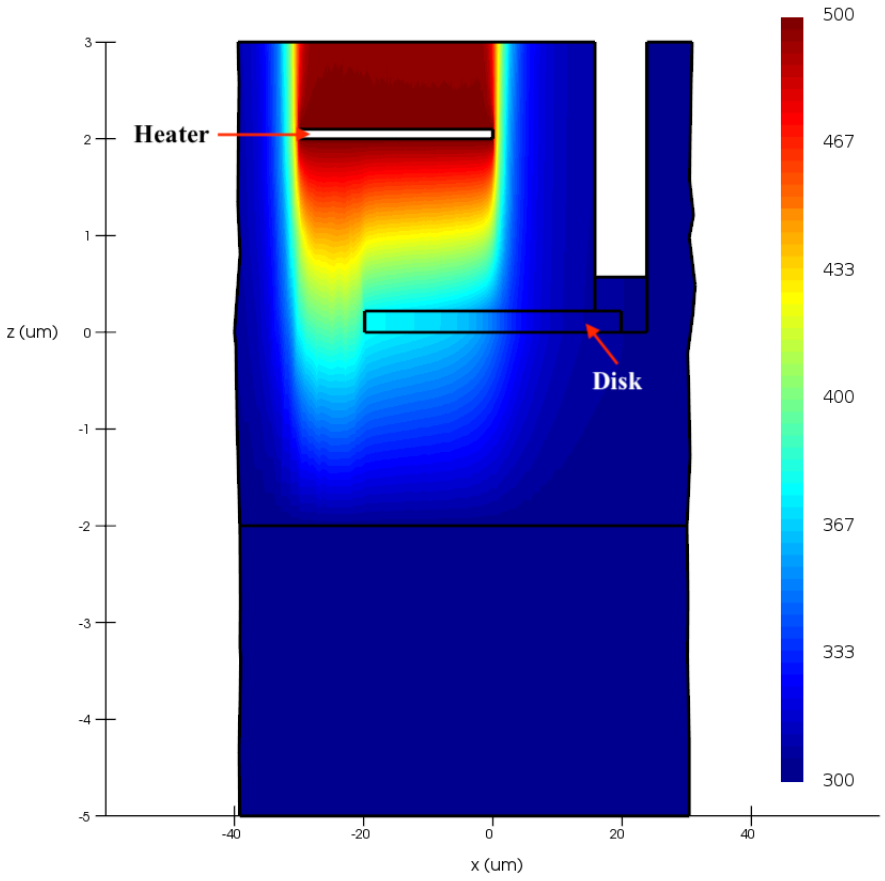

FIGURE 3.24: AA' cross-sectional view of the simulated temperature distribution for TiN heater design 2. The TiN strip has been set to a temperature of 500 K.

3.5.5 TiN heater design 3

Figures 3.25 and 3.26 illustrate the structure of the TiN heater design 3. In this design, the heater strip runs above the edge of the microdisk, which is where the disk mode is located. Since the heater strip and heater circuitry must be embedded in the foundry SiO_2 cladding, the foundry cladding above the interior of the disk is left intact. Since the mode only exists near the edge of the microdisk, the foundry cladding is only removed above the edge of the microdisk. From Figure 3.25, it is shown that the foundry oxide is removed for the outer 8 µm of the disk which is sufficient for the entire disk mode to be clad by TeO_2. The disk needs to be sufficiently large to accommodate the heater circuitry according to the constraints of the foundry process. Hence, in this design, the disk radius is chosen to be 60 μm.

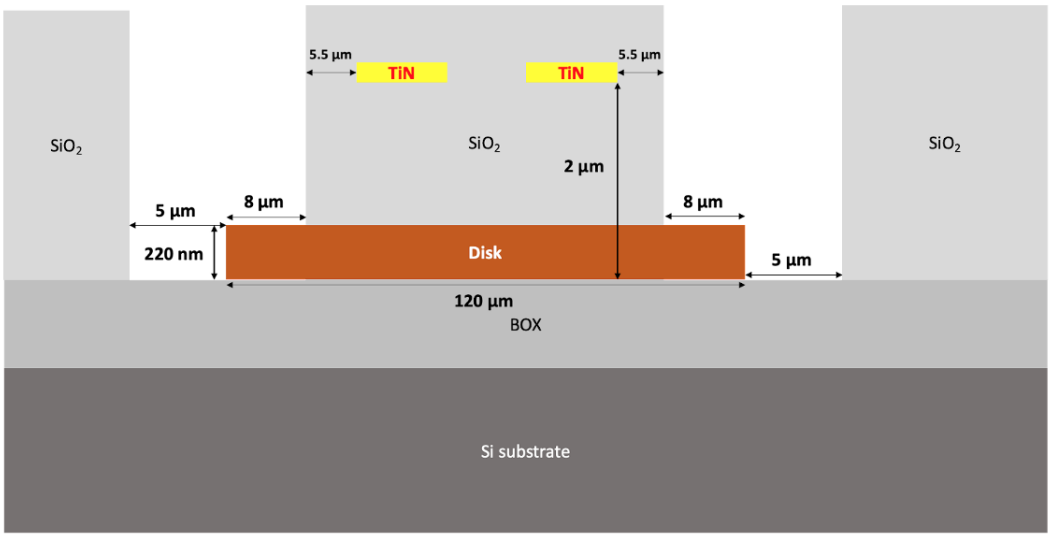

FIGURE 3.25: Cross-sectional schematic of TiN heater design 3. Heating is achieved by passing electric current through the TiN strip.

From the heatmaps in Figures 3.27 and 3.28, we can see that most of the heat

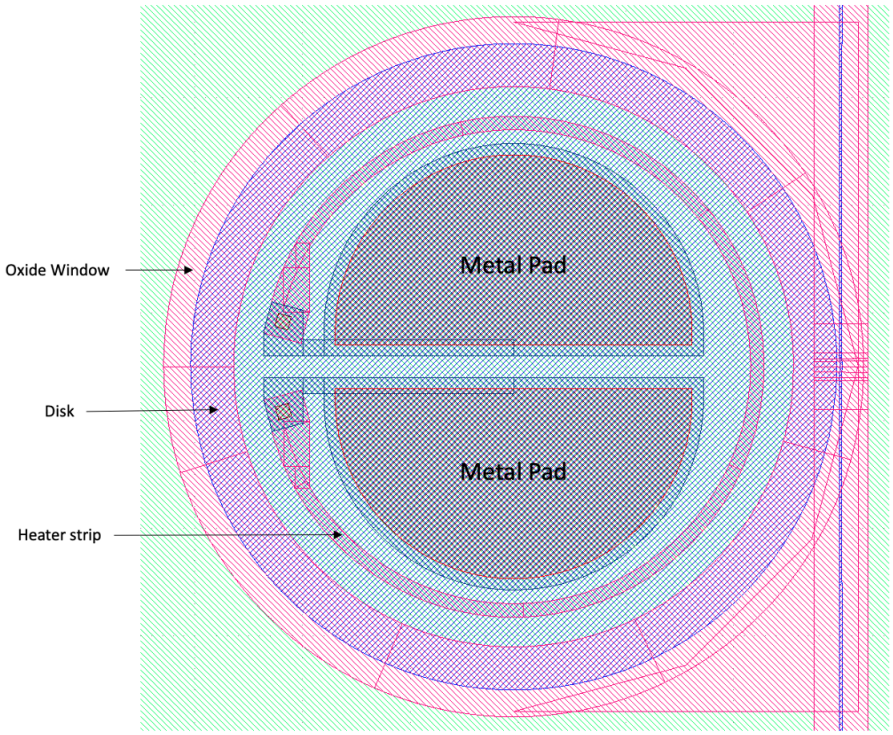

Figure 3.26: Top view schematic of TiN heater design 3

reaches the edge of the microdisk where the mode is located, since the heater is located above the edge of the disk. The edge of the disk is heated uniformly due to the circular symmetry of the heater. In contrast to the previous designs in which only roughly half the disk gets heated and contributes to resonance tuning, in this design, the entire edge of the disk gets heated and contributes to the resonance tuning. Thus, the tuning efficiency of this heater is expected to be higher than all the previous designs.

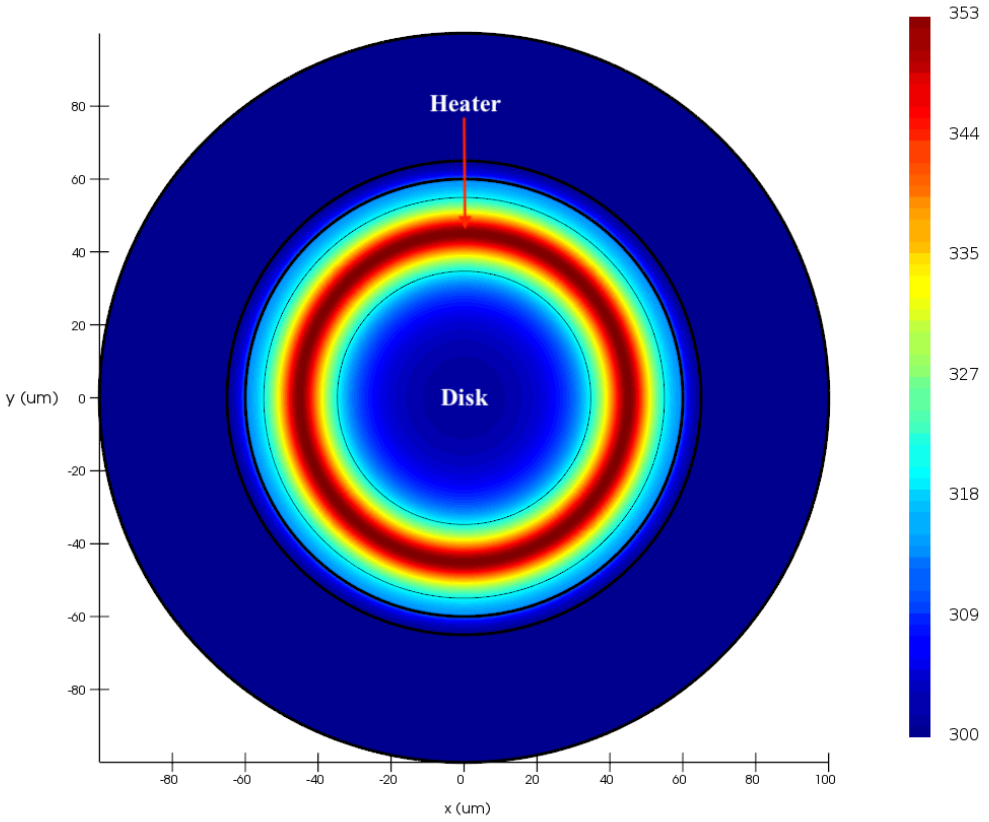

FIGURE 3.27: Top view of the simulated temperature distribution for TiN heater design 3. The TiN strip has been set to a temperature of 500 K. The black contour lines indicate a temperature of 320 K.

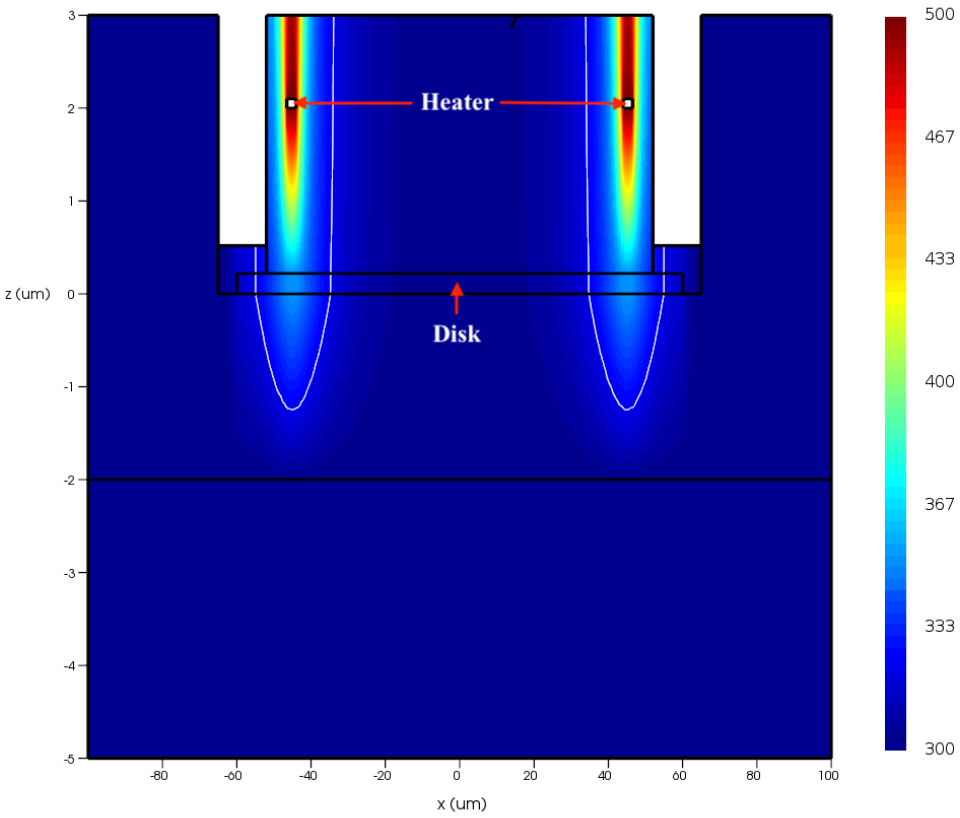

FIGURE 3.28: Cross-sectional view of the simulated temperature distribution for TiN heater design 3. The TiN strip has been set to a temperature of 500 K. The white contour line indicates a temperature of 320 K.

3.6 Summary of designs

Table 3.3 gives a summary of the characteristics, advantages and disadvantages of the heater designs discussed in this thesis. The advantages and disadvantages of the heater designs are as compared to the Si heater design 1.

Heater design	Characteristics	Advantages	Disadvantages
Si heater design 1	Doped Si strip along the edge of strip disk	Compatible with silicon microdisk laser design from [9]	Heat conduction through TeO_2 cladding is inefficient
Si heater design 2	Doped Si strip along the edge of ridge disk	Efficient heat conduction through Si slab gives high efficiency	Untested disk design for lasers
TiN heater design 1	TiN strip along the edge of disk	Separates microdisk mode and heater design	Long distance between heater and disk gives low efficiency
TiN heater design 2	TiN strip above disk with metal contacts outside disk	More heat reaches disk hence greater efficiency	Non-uniform heating, SiO_2 to TeO_2 transition increases loss
TiN heater design 3	TiN strip above disk with metal contacts above disk	Uniform heating, more heat reaches disk hence greater efficiency	Requires large disk which limits FSR

TABLE 3.3: Summary of all the heater designs

Chapter 4

Experimental Characterization and Results

In this chapter, we discuss the experimental results of the fabricated tunable microdisk resonators coated in tellurium dioxide. First, the passive results are given including the intrinsic and extrinsic Q-factors, loss and FSR which are determined from the analysis of the measured transmission data. This is followed by the resonance tuning results which are determined by observing the resonance shift for different applied heater powers. This is done for each of the heater designs presented in this thesis.

4.1 Passive microdisk measurements

Passive microdisk measurements are performed to characterize the intrinsic and extrinsic Q-factors, loss and FSR of the microdisks designed in this thesis. We measure the transmission spectra of the microdisks and extract the intrinsic and extrinsic Q-factors by fitting the dips in the transmission spectra to 2.26.

4.1.1 Passive measurement setup

We measured the transmission spectra of our fabricated SOI microdisk resonators using a fiber edge coupling setup that is illustrated in Figure 4.1. The laser used for these measurements was an Agilent tunable laser with the capability to output light in the wavelength range of 1510 nm to 1640 nm. The output of the laser was first passed through a set of polarization controllers. Next, the light was coupled into the chip bus waveguide. The light then interacted with the microdisk. The light transmitted by the microdisk was coupled into a fibre. Finally, the light was guided into a photodetector. The Agilent tunable laser source has a built in photodetector which was used to measure the transmitted power. To perform the measurement, the output of the Agilent laser was swept across its output wavelength range and the transmission at each wavelength was recorded. The Agilent laser was controlled through a GPIB connection from a laptop. A Matlab program on the laptop ran the whole experiment, from conducting the wavelength sweep to collecting and storing the data in a convenient form. The chip was placed on a stage which was in between two xyz fibre manipulators. The fibres used for coupling into and out of the chip were either lensed or cleaved fibres. The coupling was done manually by manipulating the fibres to achieve maximum transmission through the chip at a set wavelength.

4.1.2 Transmission measurements and intrinsic Q-factor results

We analyse the transmission data to extract the intrinsic Q-factor and FSR of the microdisks. The two types of microdisk designs are strip microdisks and ridge

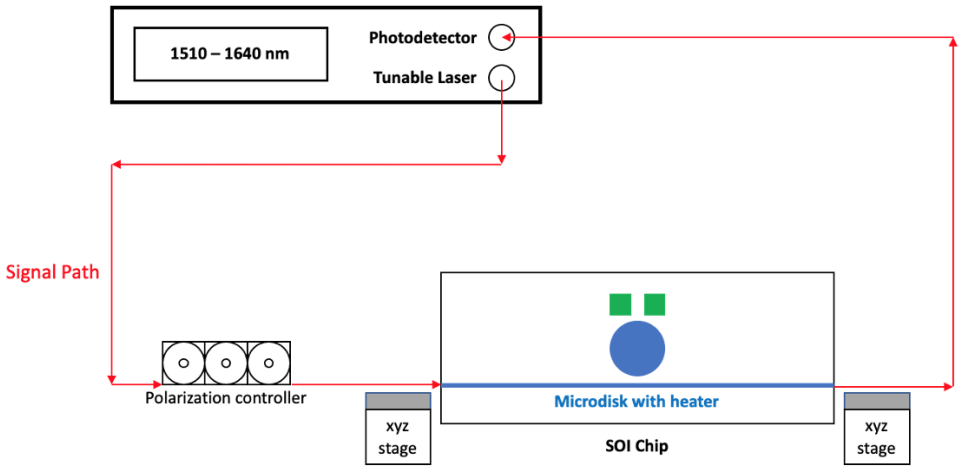

FIGURE 4.1: Experimental setup used for passive microdisk transmission measurements

microdisks. Silicon heater design 2 (Si 2) uses ridge microdisks whereas silicon heater design 1 (Si 1) and titanium nitride heater designs 1, 2 and 3 use strip microdisks. Microdisks of the same type are identical across the different heater designs. The results are presented in Table 4.1. The format of the microdisk code is as follows: Heater design, Disk radius (R), Coupling gap (G).

Microdisk code	λ (nm)	Intrinsic Q-factor	Loaded Q-factor	FSR (nm)	Loss (dB/cm)
Si 1, R=25, G=0.4	1521	2.77×10^5	1.80×10^5	4.97	1.92
Si 1, R=25, G=0.6	1627	3.99×10^5	2.96×10^5	5.00	1.42
Si 1, R=25, G=0.8	1602	4.95×10^5	4.50×10^5	4.93	1.14
Si 2, R=25, G=0.4	1607	2.99×10^5	1.73×10^5	4.83	1.93
Si 2, R=25, G=0.6	1606	2.73×10^5	1.96×10^5	4.75	2.15
Si 2, R=25, G=0.8	1612	3.78×10^5	3.44×10^5	4.73	1.57

TABLE 4.1: Summary of the passive results

Figures 4.2 and 4.3 show a sample transmission spectrum and resonance fit. The intrinsic Q-factor is extracted by fitting the dips in the transmission spectrum to Eq.(2.26). The microdisks have been designed to operate in the undercoupled

regime to $Q_0 < Q_c$. The FSR is extracted directly from the transmission spectrum by observing the spacing between consecutive resonances. However, since a microdisk has multiple modes which overlap in the transmission spectrum, we first get an estimate of the FSR from Eq.(2.21) by simulating the group index. The transmission loss in (dB/cm) is given by:

$$Loss = \frac{\lambda_{res}|10\log(\frac{1}{e})|}{Q_0 R \times FSR} = \frac{\lambda_{res} \times 4.34}{Q_0 R \times FSR} \tag{4.1}$$

where, λ_{res} = resonance wavelength in cm, Q_0 = intrinsic Q-factor, R = radius of the microdisk.

These propagation losses are comparable to those achieved in our group's previous microdisk work [9].

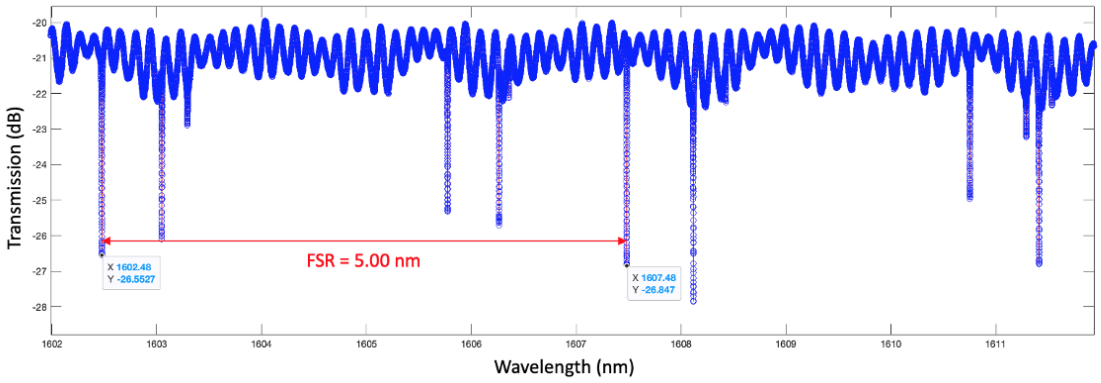

FIGURE 4.2: Sample transmission spectrum of microdisk indicating FSR

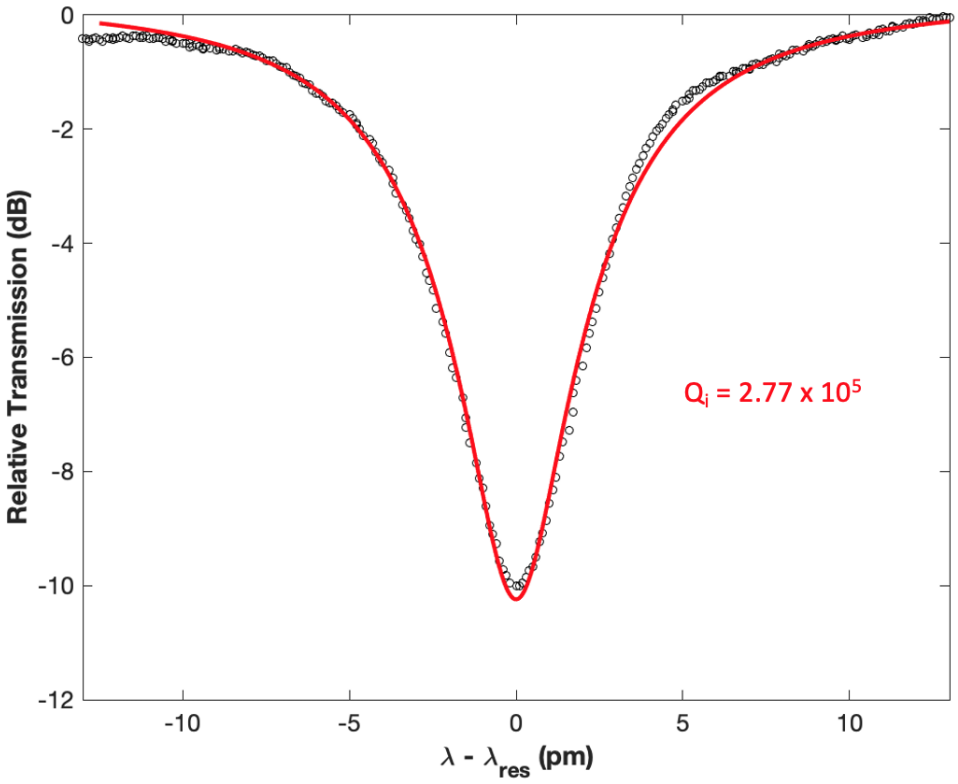

FIGURE 4.3: Sample resonance fit of microdisk indicating intrinsic Q-factor

4.2 Resonance tuning measurements

Following the characterization of the microdisks, resonance tuning measurements are performed to characterize the performance of each of the heater designs presented in this thesis. We measure the transmission spectra of the microdisks with different applied heater powers and observe the shift in the resonance wavelength of the microdisks.

4.2.1 Resonance tuning measurement setup

The experimental setup for the resonance tuning measurements, illustrated in Figure 4.4, is very similar to the one used for the passive measurements. The optical components of the setup are identical. To control the heaters, two metal probes attached to a pair of micro-manipulators are connected to a Longwei DC power supply and a Hewlett Packard multimeter. The micro-manipulators are used to place the probes on top of the metal contact pads on the chip. The metal pads get covered with TeO_2 during the sputter deposition. Hence, we use the metal probes along with the micro-manipulators to scratch the TeO_2 off the metal pads to make electrical contact with the heaters. This procedure takes some finesse and dexterity. The power source controls the voltage applied across the heater and the multimeter measures the voltage and current across the heater to measure the applied power.

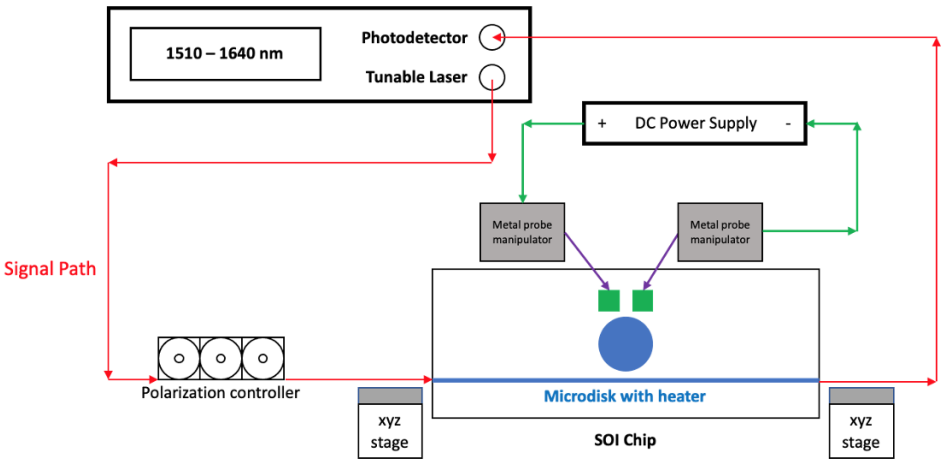

FIGURE 4.4: Experimental setup used for resonance tuning measurements

4.2.2 Analysis methodology of resonance tuning results

We characterize each heater design by measuring the microdisk transmission spectrum under various applied heater powers. We use Eq. (2.36) to calculate the efficiency, η, of each heater design. The thermo-optic coefficient, $\frac{dn_{eff}}{dT}$, is taken from the simulations presented in section 3.4. The resonance wavelength shift, $\Delta\lambda_{res}$, the resonance wavelength, λ and the FSR are taken from the measured transmission spectrum. The length of the heated part of the disk, L, is taken from the heatmaps presented in Chapter 3. The efficiency is calculated for various applied heater powers and averaged to obtain an efficiency for each heater design. Finally, the results for each heater design are compared with each other.

4.2.3 Silicon heater design 1

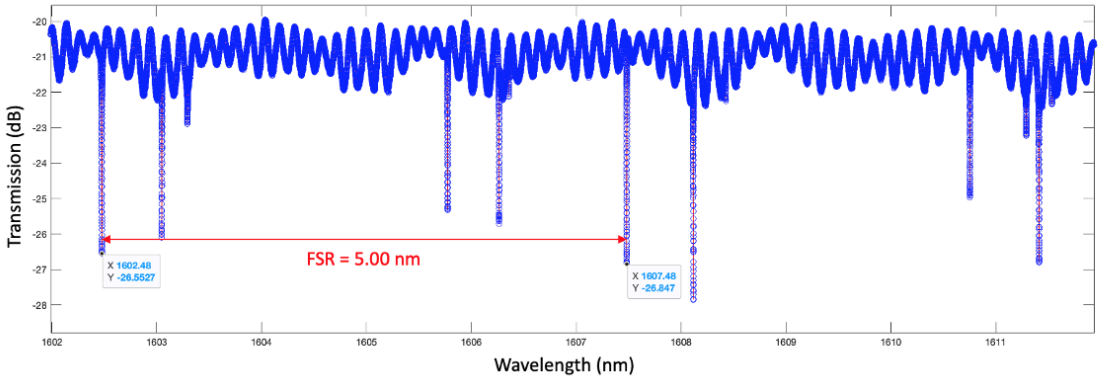

FIGURE 4.5: Transmission spectrum for Si Heater Design 1

For this design, $FSR = 5nm$, $\frac{dn_{eff}}{dT} = 1.74 \times 10^{-4}$, microdisk radius, $R = 25\mu m$, $L = \pi R$, coupling gap, $G = 0.6\mu m$ and the extinction ratio is 5.5 dB. The highest applied heater power was 20.2 mW and was supplied at an applied voltage of 10.1 V and a current of 2.00 mA. The efficiency is calculated for each of the points on the graph in Figure 4.7. The average efficiency for this heater design is $\eta = 0.458\frac{K}{mW}$.

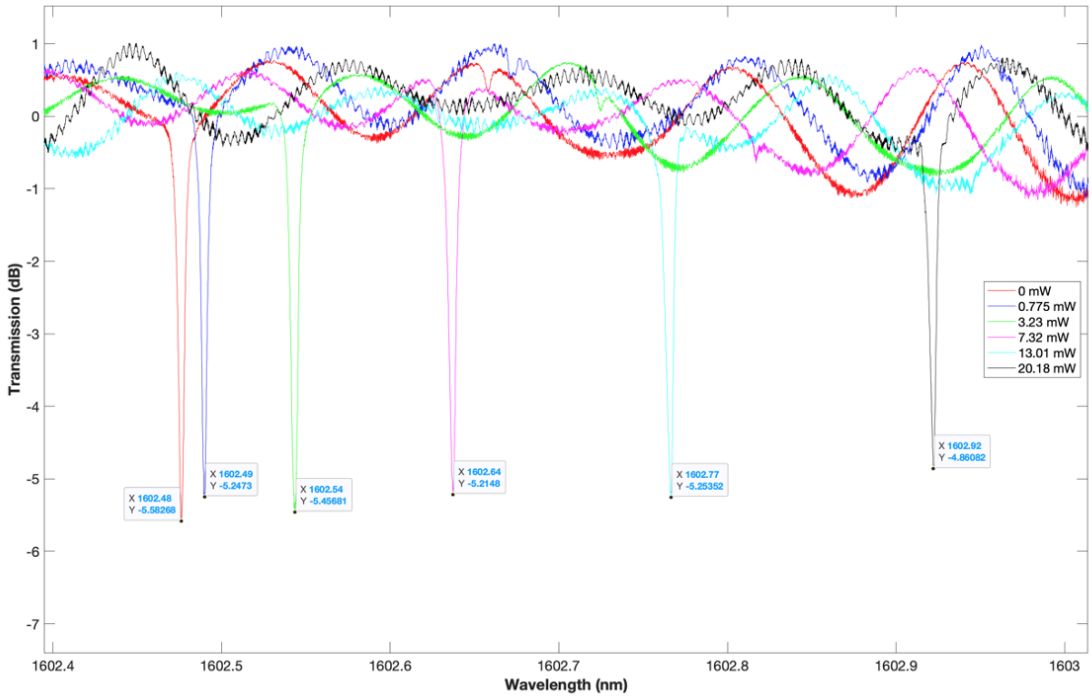

Figure 4.6: Transmission measurements of Si Heater Design 1 taken for different applied heater powers showing redshift of resonance with increasing applied heater power.

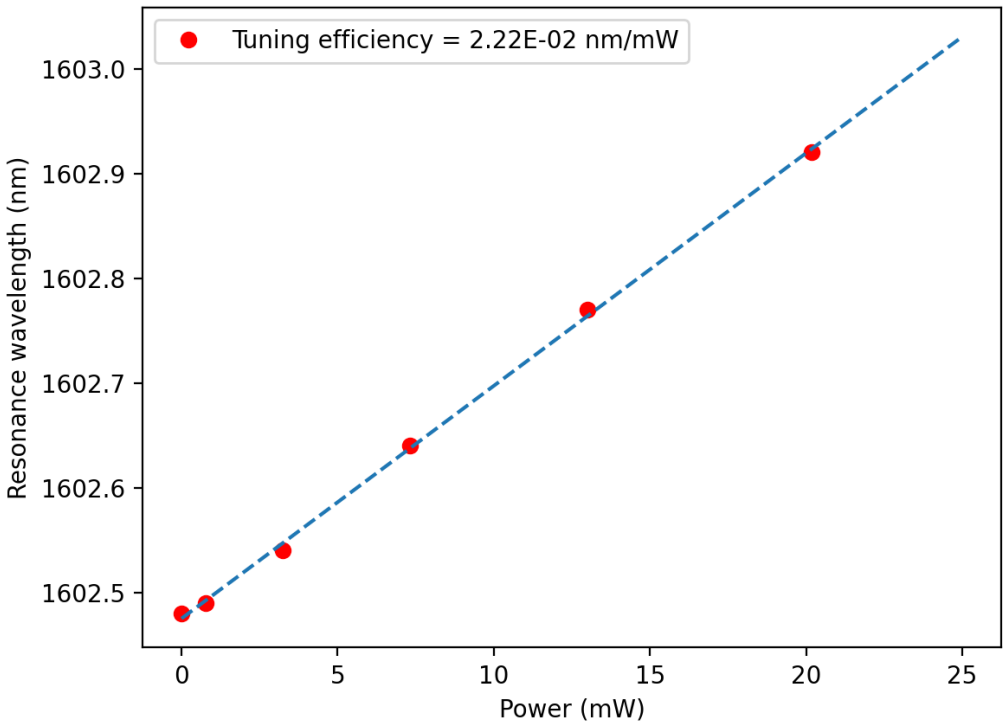

Figure 4.7: Plot of Applied heater power vs resonance wavelength for Si Heater Design 1

4.2.4 Silicon heater design 2

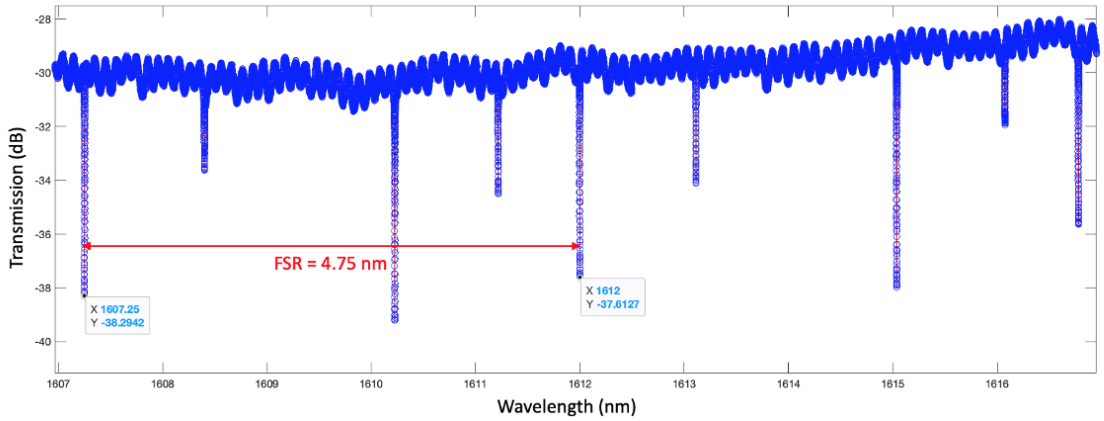

FIGURE 4.8: Transmission spectrum for Si Heater Design 2

For this design, $FSR = 4.75nm$, $\frac{dn_{eff}}{dT} = 1.74 \times 10^{-4}$, microdisk radius, $R = 25\mu m$, $L = \pi R$, coupling gap, $G = 0.6\mu m$ and the extinction ratio is 7.7 dB. The highest applied heater power was 13.5 mW and was supplied at an applied voltage of 8.01 V and a current of 1.69 mA. The efficiency is calculated for each of the points on the graph in Figure 4.10. The average efficiency for this heater design is $\eta = 1.112\frac{K}{mW}$.

We observe resonance splitting in the transmission spectra for non-zero applied heater power, as shown in Figure 4.11. The splitting gets more pronounced for higher heater powers. This might be attributed to reflection when light crosses from the heated part of the disk to the non-heated part of the disk and vice versa [21, 29]. In this design, heat is conducted to the disk more efficiently than compared to other designs. Since the disk heats up much more in this design than compared to the other designs, there is a significant difference between the refractive index of the heated part of the disk and the non-heated part of the disk.

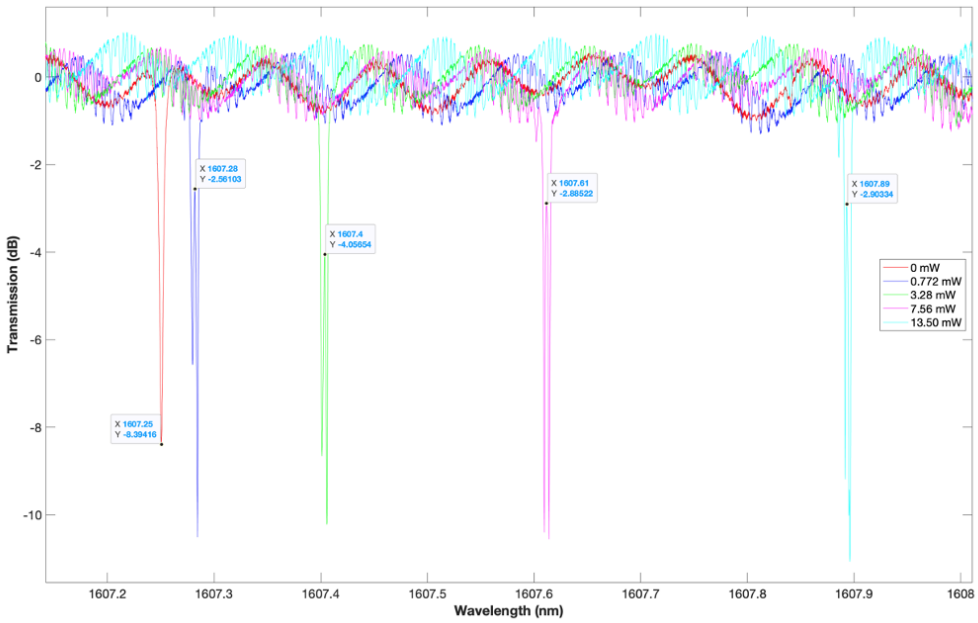

Figure 4.9: Transmission measurements of Si Heater Design 2 taken for different applied heater powers showing redshift of resonance with increasing applied heater power.

This can lead to reflection, but further investigation is required to confirm the source of the resonance splitting.

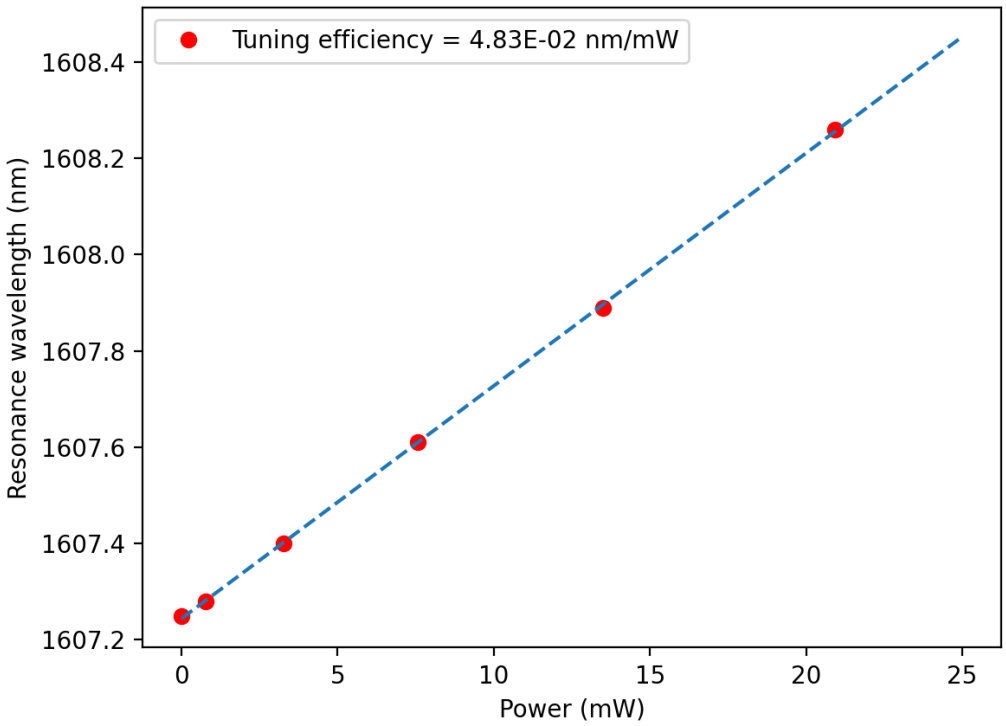

FIGURE 4.10: Plot of Applied heater power vs resonance wavelength for Si Heater Design 2

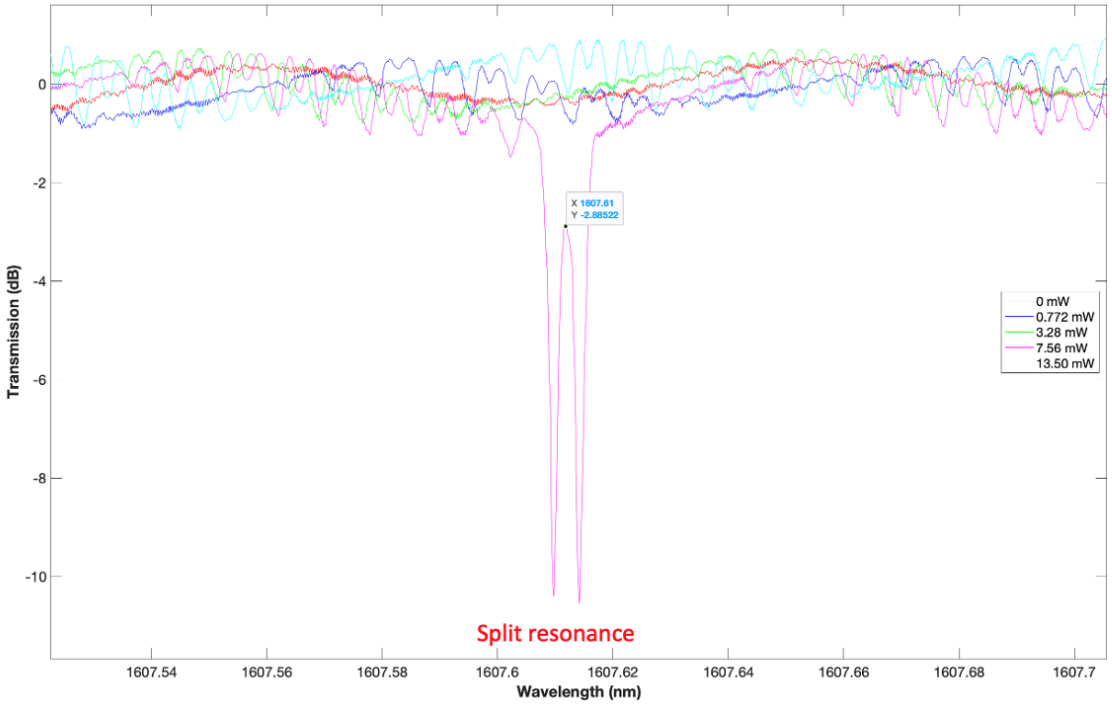

FIGURE 4.11: Split resonance resulting from reflection due to refractive index difference between heated and non-heated part of disk

4.2.5 TiN heater design 1

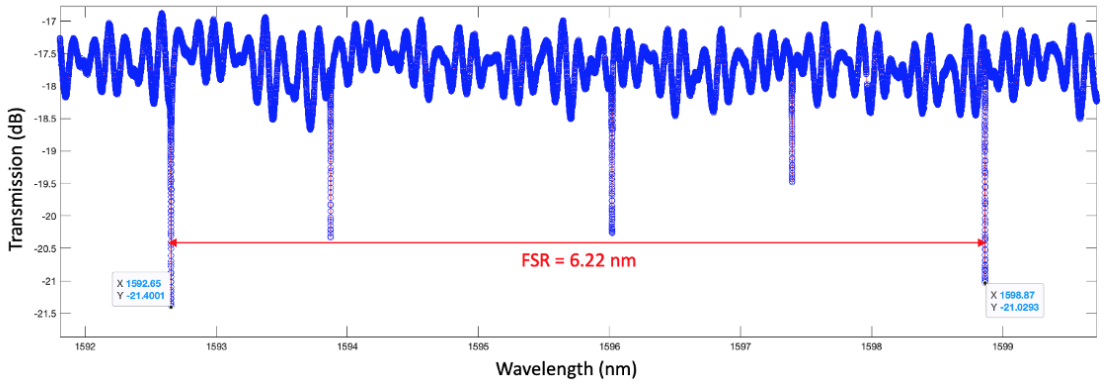

FIGURE 4.12: Transmission spectrum for TiN Heater Design 1

For this design, $FSR = 6.22nm$, $\frac{dn_{eff}}{dT} = 1.74 \times 10^{-4}$, microdisk radius, $R = 20\mu m$, $L = \pi R$, coupling gap, $G = 0.6\mu m$ and the extinction ratio is 3.6 dB. The highest applied heater power was 75.8 mW and was supplied at an applied voltage of 6.02 V and a current of 12.6 mA. The efficiency is calculated for each of the points on the graph in Figure 4.14. The average efficiency for this heater design is $\eta = 0.145\frac{K}{mW}$.

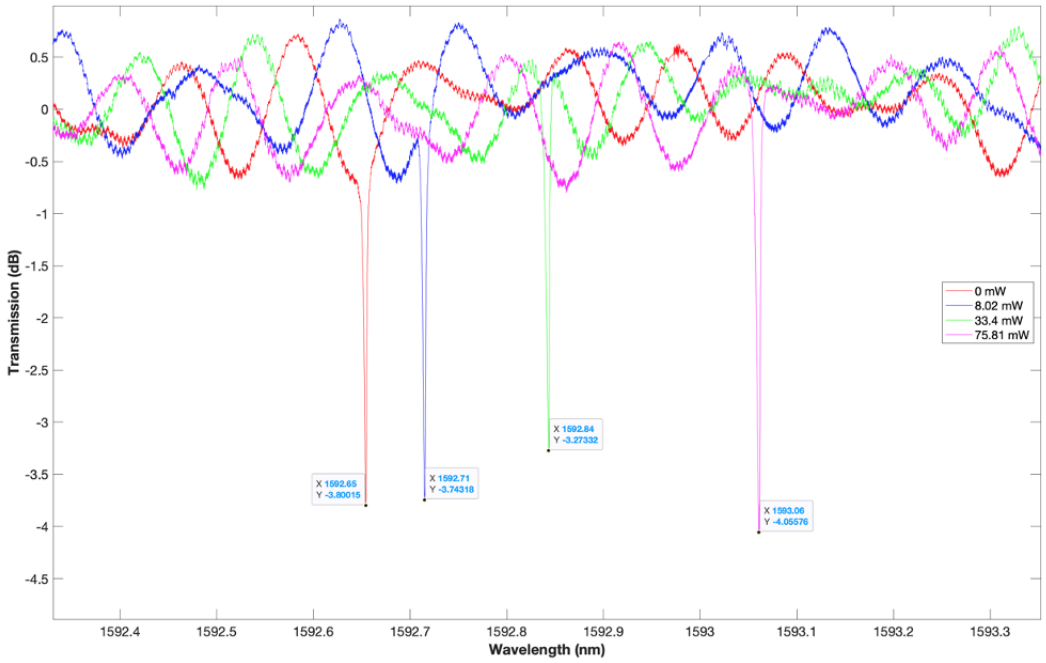

Figure 4.13: Transmission measurements of TiN Heater Design 1 taken for different applied heater powers showing redshift of resonance with increasing applied heater power.

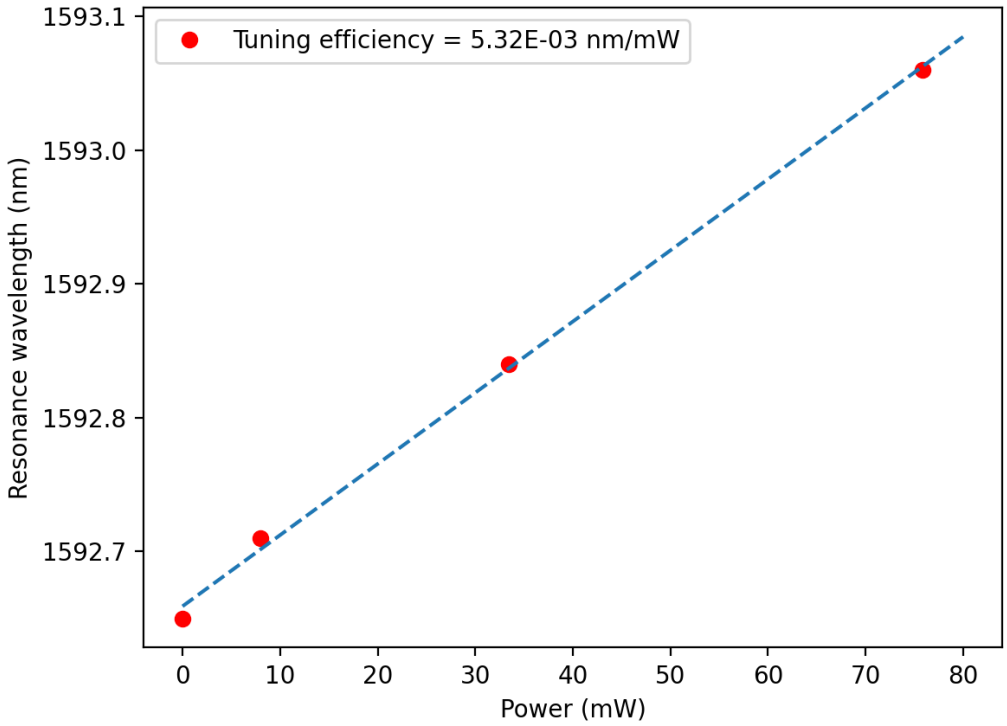

Figure 4.14: Plot of Applied heater power vs resonance wavelength for TiN Heater Design 1

4.2.6 TiN heater design 2

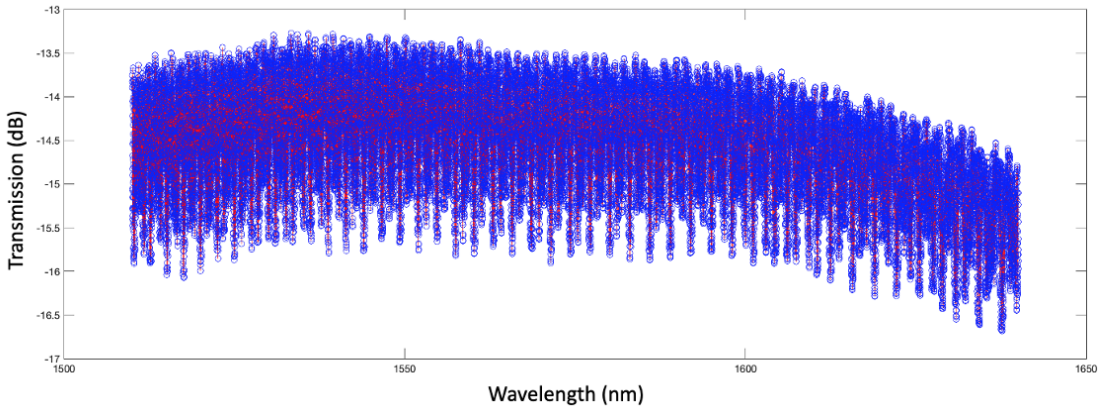

FIGURE 4.15: Transmission spectrum for TiN Heater Design 2

No resonances were observed for these disk designs. In this disk, there are transitions from the SiO_2 cladding to the TeO_2 cladding at two points. This leads to reflections and mode-mismatch losses. The transitions were tapered in an attempt to reduce these losses. However, from the lack of resonances in the transmission spectrum for all waveguide-microdisk gaps, it can be concluded that the losses were still significant.

4.2.7 TiN heater design 3

For this design, $FSR = 2.02nm$, $\frac{dn_{eff}}{dT} = 1.74 \times 10^{-4}$, microdisk radius, $R = 60\mu m$, $L = 2\pi R$, coupling gap, $G = 0.6\mu m$ and the extinction ratio is 3.0 dB. The highest applied heater power was 30.2 mW and was supplied at an applied voltage of 6.02 V and a current of 5.02 mA. The efficiency is calculated for each of the points on the graph in Figure 4.18. The average efficiency for this heater design is $\eta = 0.251 \frac{K}{mW}$.

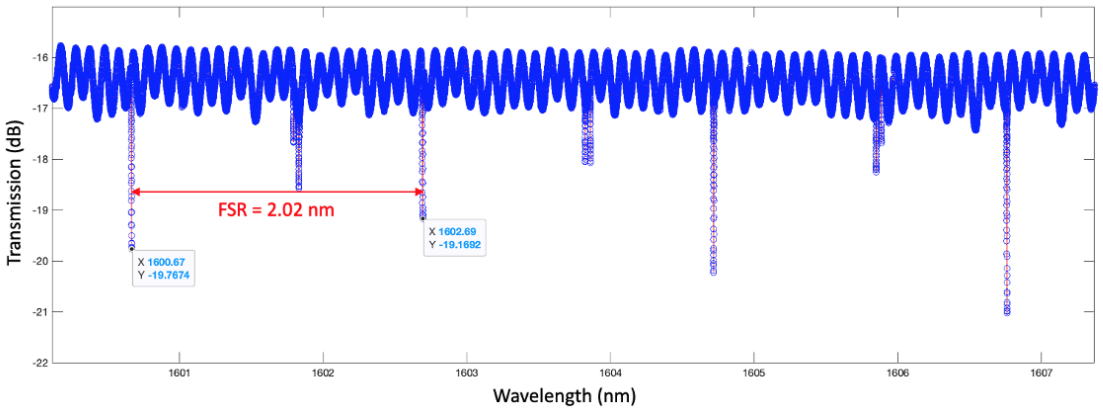

Figure 4.16: Transmission spectrum for TiN Heater Design 3

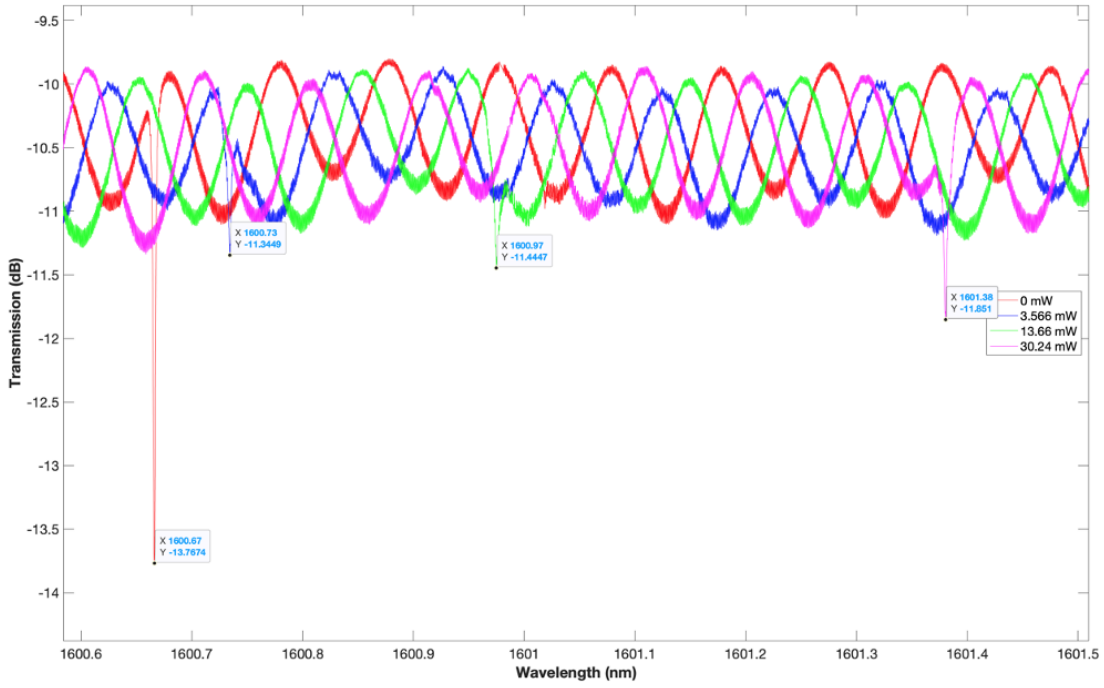

Figure 4.17: Transmission measurements of TiN Heater Design 3 taken for different applied heater powers showing redshift of resonance with increasing applied heater power.

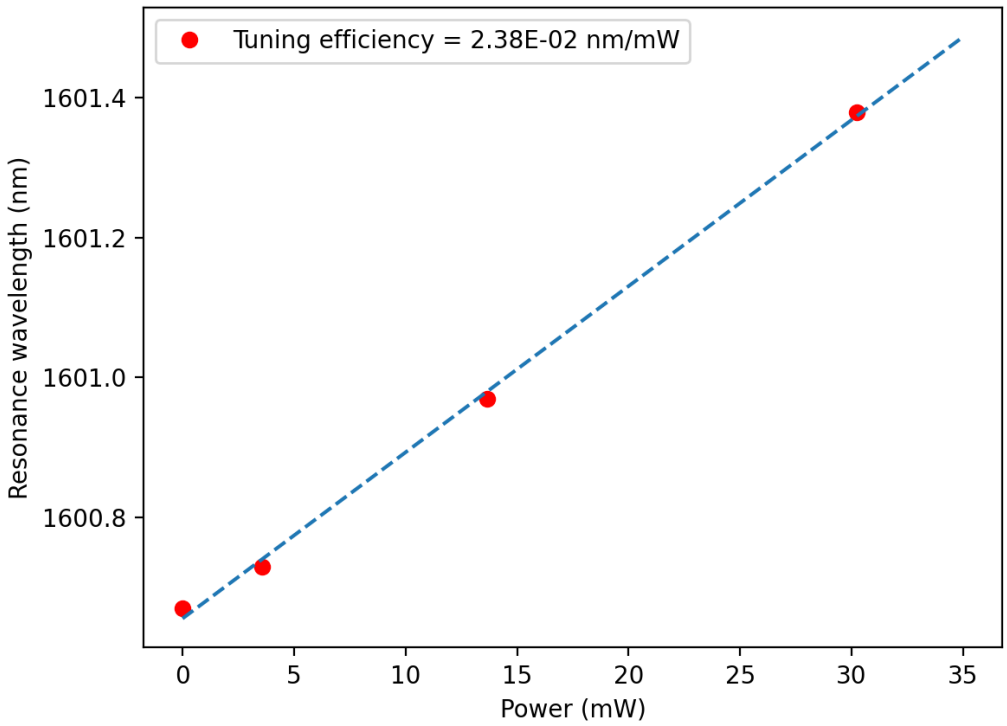

Figure 4.18: Plot of Applied heater power vs resonance wavelength for TiN Heater Design 3

4.2.8 Comparison of different heater designs

Table 4.2 summarizes the heater tuning performance of all the heater designs. The Si Heater Design 2 has the best performance. It is over 2 times more efficient than the Si Heater Design 1 by both metrics. In Chapter 3, the theoretical upper limit for the efficiencies of Si Heater Designs 1 and 2 as a percentage of the applied heater power were calculated to be 1.7 % and 40 % respectively. The experimental results agree with the theoretical estimates that the Si Heater Design 2 has a much higher efficiency than the Si Heater Design 1.

Heater Design	Tuning efficiency (nm/mW)	Heating efficiency, η (K/mW)
Si Heater Design 1	2.22×10^{-2}	0.458
Si Heater Design 2	4.83×10^{-2}	1.11
TiN Heater Design 1	0.532×10^{-2}	0.145
TiN Heater Design 2	N/A	N/A
TiN Heater Design 3	2.38×10^{-2}	0.251

TABLE 4.2: Summary of the resonance tuning results

The TiN Heater Design 1 has the lowest performance. This makes sense since the heater in this design is located very far from the disk due to the constraints of the foundry process.

The performance of the TiN Heater Design 3 is comparable to the performance of the Si Heater Design 1. The heating efficiency, η, of the TiN Heater Design 3 is about half that of the Si Heater Design 1. However, in the TiN Heater Design 3, the entire circumference of the disk is heated as compared to only half the circumference being heated in the Si Heater Design 1. Furthermore, the radius of the disk in the TiN Heater design 3 is 60 μm whereas the radius of the disk in the Si Heater Design 1 is 25 μm. Hence, the length of the light path that is heated in

the TiN Heater Design 3 is about five times than that of the one in the Si Heater Design 1. The longer length of the heated path compensates for the lower heating efficiency resulting in roughly the same tuning efficiency for both designs.

In Table 4.3, the performance of previously demonstrated thermally tuned silicon resonators with various heater designs is compared with the performance of the devices presented in this thesis. In Geng et all [36], the heater is located 1.2 μm above the ring resonator with SiO_2 cladding in between and has a tuning efficiency of 0.1616 nm/mW. Our device that has the most similarity with this heater design is the TiN Heater Design 3 which has a tuning efficiency of 0.0238 nm/mW. The reason that the tuning efficiency of our device is an order of magnitude lower is twofold. Firstly, in our device, the oxide cladding between the heater and the silicon microdisk is thicker at 2 μm. This reduces the amount of heat that reaches the microdisk. More importantly, in our device, the heater is not positioned above the edge of the microdisk where the mode is located but rather $\approx$ 15 μm away from the edge of the disk. As can be seen from Figure 3.28, the edge of the disk does not heat up nearly as much as the part of the disk directly below the heater. This is the main reason for the lower tuning efficiency of our device.

In Watts et all [37], the resonator is a microdonut with an outer radius of 3 μm where the inner edge of the donut is doped to form a silicon heater. The close proximity of the heater to the resonator mode and the high thermal conductivity of silicon combined with the small size of the resonator leads to a very high tuning efficiency of 1.82 nm/mW. In [38] and [39], complicated fabrication processes such as deep trenching and undercutting are used to insulate the heater and resonator from heat sinks, thus retaining more heat in the resonator and improving tuning

Heater Type	Tuning efficiency (nm/mW)
Metal heater atop SiO_2 cladding [36]	0.1616
Doped silicon heater [37]	1.82
Metal heater with air trench [38]	0.909
Metal heater with air trench + undercutting [39]	2.7
Graphene heaters directly atop Si microdisk [40]	0.48
This thesis: Si Heater Design 2	0.0483

TABLE 4.3: Comparison of tuning efficiency between previously demonstrated thermally tuned silicon resonators and the best device presented in this thesis

efficiency. However, these fabrication techniques are not available in many photonics foundries. In [40], graphene heaters are positioned directly atop a silicon microdisk which results in efficient heating of the mirodisk and a high tuning efficiency. However, graphene is not available currently in many silicon photonics foundries.

The goal of this research is to design tunable microdisk lasers. For this application, the ability to shift a resonance by one complete FSR is highly desirable. The highest tuning efficiency among the designed devices is that of the Si Heater Design 2 which has a tuning efficiency of 0.0483 nm/mW. The radius of the microdisk is 25 μm and its FSR is 4.75 nm. In order to shift the resonance by one complete FSR, the required heater power is 98 mW, which is extremely high. Hence, the tuning efficiency needs to be greatly improved for the purpose of this application.

Chapter 5

Conclusion

5.1 Thesis overview

The objective of this project was to fabricate and characterize thermally tuned hybrid TeO_2-Si microdisk resonators. The goal was to develop heater designs that are compatible with standard silicon foundry processes and our TeO_2 deposition post-processing step to enable the tuning of on-chip lasers. Several heater designs were developed and their resonance tuning performance was measured and compared.

The Lumerical MODE and HEAT simulation software packages were used in the design phases of the project to simulate the mode profiles and thermo-optic coefficients of the microdisk resonators and the heating profiles of the various heater designs. A design mask was created using Luceda IPKISS Photonics Design Platform. The design mask was sent to the AMF silicon photonics foundry to fabricate the designed devices. TeO_2 was deposited on the fabricated chips using

magnetron reactive sputtering at McMaster University in a single post-processing step.

Following the TeO_2 deposition, experimental measurements were carried out to characterize the devices. First, passive transmission measurements of the silicon microdisks were performed to extract their intrinsic Q-factors, loss in dB/cm and FSR. The highest intrinsic Q-factor and hence, lowest propagation loss measured was 4.95×10^5 and 1.14 dB/cm respectively. This loss is comparable to the one measured in Khadijeh et al. [9]. The results are highlighted in Table 4.1. This is followed by resonance tuning measurements to characterize the tuning efficiencies of each of the heater designs presented in this thesis. Si Heater Design 2 was measured to have the highest tuning efficiency of 0.0483 nm/mW. The results are highlighted in Table 4.2.

5.2 Future work

Based on the resonance tuning results, several design decisions may be taken to improve the tuning efficiency of our heaters. To improve the tuning efficiency of the silicon heater designs, we can change the microdisk to a micro-donut resonator. This will greatly reduce the amount of heat conducted away from the edge of the disk, where the mode exists, towards the interior of the disk. Since more heat will be retained near the edge of the disk, the tuning efficiency should be improved. We can also alter the geometry of the heater strips to heat the entire edge of the disk rather than just one half. The longer heated light path will increase the tuning efficiency of the heaters. Furthermore, this has the additional benefit of heating

the disk more uniformly and thus, eliminating unwanted reflections and resonance splitting.

The passive transmission measurements of the silicon microdisks demonstrated intrinsic Q-factors and losses that are comparable to those obtained in the group's previous laser work [9]. Hence, a straightforward extension of this project is to deposit rare-earth doped TeO_2 onto these chips with the goal of creating on-chip tunable lasers which have several applications. The resonance wavelength of a tunable microdisk laser can be tuned to match the pump wavelength provided by an external laser which allows us to pump the on-chip laser without the use of an expensive tunable pump laser. We can also tune multiple on-chip microdisk lasers with slightly different disk radii to the same pump wavelength to produce different emission wavelengths and create a WDM source.

5.3 Skills acquired

I acquired a great number of skills over the course of this project. I gained valuable understanding of various computational methods such as the finite element method, the finite difference method and the finite difference time domain method that were used to simulate and design the devices presented in this thesis. I gained exposure to various commercial simulation software packages such as Lumerical MODE and HEAT that were used to design the devices presented in this thesis. Other software based skills that were gained include design mask layout and GDS creation using Luceda IPKISS Photonics Design Platform and KLayout. These skills were gained through attending the Passive Silicon Photonics Fabrication Course offered through the NSERC Silicon Electronic-Photonic Integrated

Circuits (SiEPIC) program that is hosted by CMC Microsystems. Practical laboratory skills gained include the use of optical and fiber optic equipment to make measurements, the use of xyz-stages to edge couple light from fibres onto chips and place metal probes on chips to make electrical contact with on-chip devices.

Bibliography

[1] D. Thomson, A. Zilkie, J. E. Bowers, T. Komljenovic, G. T. Reed, L. Vivien, D. Marris-Morini, E. Cassan, L. Virot, J.-M. Fédéli, J.-M. Hartmann, J. H. Schmid, D.-X. Xu, F. Boeuf, P. O'Brien, G. Z. Mashanovich, and M. Nedeljkovic. "Roadmap on silicon photonics". *Journal of Optics* 18(7) (2016), 1–20.

[2] Q. Xu, B. Schmidt, S. Pradhan, and M. Lipson. "Micrometre-scale silicon electro-optic modulator". *Nature* 435 (2005), 325–327.

[3] G. T. Reed. "The optical age of silicon". *Nature* 427 (2004), 595–596.

[4] S. Keyvaninia, S. Verstuyft, L. V. Landschoot, F. Lelarge, G. .-. Duan, S. Messaoudene, J. M. Fedeli, T. D. Vries, B. Smallbrugge, E. J. Geluk, J. Bolk, M. Smit, G. Morthier, D. V. Thourhout, and G. Roelkens. "Heterogeneously integrated III-V/silicon distributed feedback lasers". *Optics Letters* 38(24) (2013), 5434–5437.

[5] A. Y. Liu, R. W. Herrick, O. Ueda, P. M. Petroff, A. C. Gossard, and J. E. Bowers. "Reliability of InAs/GaAs Quantum Dot Lasers Epitaxially Grown on Silicon". *IEEE Journal of Selected Topics in Quantum Electronics* 21(6) (2015).

[6] O. Boyraz and B. Jalali. "Demonstration of a silicon Raman laser". *Optics Express* 12(21) (2004), 5269–5273.

[7] H. Rong, A. Liu, R. Jones, O. Cohen, D. Hak, R. Nicolaescu, A. Fang, and M. Paniccia. "An all-silicon Raman laser". *Nature* 433 (2005), 292–294.

[8] M. Ahmadi, W. Shi, and S. LaRochelle. "Widely tunable silicon Raman laser". *Optica* 8(6) (2021), 804–810.

[9] K. M. Kiani, H. C. Frankis, C. M. Naraine, D. B. Bonneville, A. P. Knights, and J. D. B. Bradley. "Lasing in a Hybrid Rare-Earth Silicon Microdisk". *Laser and Photonics Reviews* 16(1) (2022).

[10] C. Naraine. "Fabrication, Design and Characterization of Silicon-on-Insulator Waveguide Amplifiers Coated in Erbium-Doped Tellurium Oxide". Master's Thesis. McMaster University, 2020.

[11] A. Jha, B. Richards, G. Jose, T. Teddy-Fernandez, P. Joshi, X. Jiang, and J. Lousteau. "Rare-earth ion doped TeO_2 and GeO_2 glasses as laser materials". *Progress in Materials Science* 57(8) (2012), 1426–1491.

[12] H. C. Frankis, K. M. Kiani, D. B. Bonneville, C. Zhang, S. Norris, R. Mateman, A. Leinse, N. D. Bassim, A. P. Knights, and J. D. B. Bradley. "Low-Loss TeO_2-coated Si_3N_4 waveguides for application in photonic integrated circuits". *Optics Express* 27(9) (2019), 12529–12540.

[13] S. J. Madden and K. T. Vu. "Very low loss reactively ion etched Tellurium Dioxide planar rib waveguides for linear and non-linear optics". *Optics Express* 17(20) (2009), 17645–17651.

[14] K. Vu and S. Madden. "Tellurium dioxide Erbium doped planar rib waveguide amplifiers with net gain and 2.8 dB/cm internal gain". *Optics Express* 18(18) (2010), 19192–19200.

[15] K. Vu, S. Farahani, and S. Madden. "980 nm pumped erbium doped tellurium oxide planar rib waveguide laser and amplifier with gain in S, C and L band". *Optics Express* 23(2) (2015), 747–755.

[16] H. C. Frankis, K. M. Kiani, D. Su, R. Mateman, A. Leinse, and J. D. B. Bradley. "High-Q tellurium-oxide-coated silicon nitride microring resonators". *Optics Letters* 44(1) (2019), 118–121.

[17] J. H. Schmid, A. Delâge, B. Lamontagne, J. Lapointe, S. Janz, P. Cheben, A. Densmore, P. Waldron, D. .-. Xu, and K. P. Yap. "Interference effect in scattering loss of high-index-contrast planar waveguides caused by boundary reflections". *Optics Letters* 33(13) (2008), 1479–1481.

[18] C. M. Naraine, J. W. Miller, H. C. Frankis, D. E. Hagan, P. Mascher, J. H. Schmid, P. Cheben, A. P. Knights, and J. D. B. Bradley. "Subwavelength grating metamaterial waveguides functionalized with tellurium oxide cladding". *Optics Express* 28(12) (2020), 18538–18547.

[19] K. M. Kiani, H. C. Frankis, H. M. Mbonde, R. Mateman, A. Leinse, A. P. Knights, and J. D. B. Bradley. "Thulium-doped tellurium oxide waveguide amplifier with 7.6 dB net gain on a silicon nitride chip". *Optics Letters* 44(23) (2019), 5788–5791.

[20] H. C. Frankis, H. M. Mbonde, D. B. Bonneville, C. Zhang, R. Mateman, A. Leinse, and J. D. B. Bradley. "Erbium-doped TeO_2-coated Si_3N_4 waveguide amplifiers with 5 dB net gain". *Photonics Research* 8(2) (2020), 127–134.

[21] W. Bogaerts, P. D. Heyn, T. V. Vaerenbergh, K. D. Vos, S. K. Selvaraja, T. Claes, P. Dumon, P. Bienstman, D. V. Thourhout, and R. Baets. "Silicon microring resonators". *Laser and Photonics Reviews* 6(1) (2012), 47–73.

[22] T. Barwicz, H. Byun, F. Gan, C. W. Holzwarth, M. A. Popovic, P. T. Rakich, M. R. Watts, E. P. Ippen, F. X. Kärtner, H. I. Smith, J. S. Orcutt, R. J. Ram, V. Stojanovic, O. O. Olubuyide, J. L. Hoyt, S. Spector, M. Geis, M. Grein, T. Lyszczarz, and J. U. Yoon. "Silicon photonics for compact, energy-efficient interconnects". *Journal of Optical Networking* 6(1) (2007), 63–73.

[23] K. D. Vos, J. Girones, S. Popelka, E. Schacht, R. Baets, and P. Bienstman. "SOI optical microring resonator with poly(ethylene glycol) polymer brush for label-free biosensor applications". *Biosensors and Bioelectronics* 24(8) (2009), 2528–2533.

[24] G. Choo, C. K. Madsen, S. Palermo, and K. Entesari. "Automatic Monitor-Based Tuning of an RF Silicon Photonic 1X4 Asymmetric Binary Tree True-Time-Delay Beamforming Network". *Journal of Lightwave Technology* 36(22) (2018), 5263–5275.

[25] K. M. Kiani, H. M. Mbonde, H. C. Frankis, R. Mateman, A. Leinse, A. P. Knights, and J. D. B. Bradley. "Four-wave mixing in high-Q tellurium-oxide-coated silicon nitride microring resonators". *OSA Continuum* 3(12) (2020), 3497–3507.

[26] S. Liu, J. Feng, Y. Tian, H. Zhao, L. Jin, B. Ouyang, J. Zhu, and J. Guo. "Thermo-optic phase shifters based on silicon-on-insulator platform: state-of-the-art and a review". *Frontiers of Optoelectronics* 15(9) (2022).

[27] J. Heebner, R. Grover, and T. A.Ibrahim. *Optical Microresonators: Theory, Fabrication and Applications*. Springer, 2008.

[28] G. Keiser. *Optical Fiber Communications*. Second Edition. McGraw-Hill, 1991.

[29] M. Soltani. "Novel Integrated Silicon Nanophotonic Structures using Ultra-high Q Resonators". PhD Thesis. Georgia Institute of Technology, 2009.

[30] R. Nayak, V. Gupta, A. L. Dawar, and K. Sreenivas. "Optical waveguiding in amorphous tellurium oxide thin films". *Thin Solid Films* 445 (2003), 118–126.

[31] S. M. Pietralunga, M. Lanata, M. Ferè, D. Piccinin, G. Cusmai, M. Torregiani, and M. Martinelli. "High-contrast waveguides in sputtered pure TeO_2 glass thin films". *Optics Express* 16(26) (2008), 21662–21670.

[32] A. W. Elshaari, I. E. Zadeh, K. D. Jöns, and V. Zwiller. "Thermo-Optic Characterization of Silicon Nitride Resonators for Cryogenic Photonic Circuits". *IEEE Photonics Journal* 8(3) (2016).

[33] H. Li, J. Lousteau, W. N. MacPherson, X. Jiang, H. T. Bookey, J. S. Barton, A. Jha, and A. K. Kar. "Thermal sensitivity of tellurite and germanate optical fibers". *Optics Express* 15(14) (2007), 8857–8863.

[34] M. D. Ewbank and P. R. Newman. "Temperature dependence of the thermal conductivity for tellurium dioxide". *Solid State Communications* 39(2) (1981), 303–305.

[35] F. P. Incropera and D. P. DeWitt. *Fundamentals of Heat and Mass Transfer*. Fourth Edition. Wiley, 1996.

[36] M. Geng, L. Jia, L. Zhang, L. Yang, P. Chen, T. Wang, and Y. Liu. "Four-channel reconfigurable optical add-drop multiplexer based on photonic wire waveguide". *Optics Express* 17(7) (2009), 5502–5516.

[37] M. R. Watts, W. A. Zortman, D. C. Trotter, G. N. Nielson, D. L. Luck, and R. W. Young. "Adiabatic Resonant Microrings (ARMs) with directly integrated thermal microphotonics". In: *Conference on Lasers and Electro-Optics*. 2009.

[38] P. Dong, W. Qian, H. Liang, R. Shafiiha, N.-N. Feng, D. Feng, X. Zheng, A. V. Krishnamoorthy, and M. Asghari. "Low power and compact reconfigurable multiplexing devices based on silicon microring resonators". *Optics Express* 18(10) (2010), 9852–9858.

[39] P. Dong, W. Qian, H. Liang, R. Shafiiha, D. Feng, G. Li, J. E. Cunningham, A. V. Krishnamoorthy, and M. Asghari. "Thermally tunable silicon racetrack resonators with ultralow tuning power". *Optics Express* 18(19) (2010), 20298–20304.

[40] L. Yu, Y. Yin, Y. Shi, D. Dai, and S. He. "Thermally tunable silicon photonic microdisk resonator with transparent graphene nanoheaters". *Optica* 3(2) (2016), 159–166.